optics

MDPI

Article

Performance Analysis of RIS-Assisted Modulating Retroreflector Underwater Optical Wireless Communication with Diversity Combining

Amr G. AbdElKader [1,2,*], Ahmed Allam [3], Hossam M. Shalaby [4] and Kazutoshi Kato [1,*]

[1] Graduate School of Information Science and Electrical Engineering, Kyushu University, Fukuoka 819-0395, Japan
[2] Faculty of Engineering, Alexandria University, Alexandria 21544, Egypt
[3] Department of Electronics and Communications Engineering, Egypt-Japan University of Science and Technology (E-JUST), Alexandria 21934, Egypt
[4] Department of Electrical Engineering and Computer Science, University of Toledo, Toledo, OH 43606, USA; shalaby@ieee.org
* Correspondence: abdelkader.amr.026@m.kyushu-u.ac.jp (A.G.A.); kato@ed.kyushu-u.ac.jp (K.K.)

Abstract

Reconfigurable intelligent surfaces (RISs) have recently attracted attention as a potential solution for improving the reliability of optical wireless communication links, especially when direct transmission (DT) becomes severely degraded due to dynamic channel conditions. In this study, an RIS-assisted architecture based on a modulating retroreflector is proposed for underwater optical wireless communications (MRR-UOWC). In the considered system, both the DT path and the RIS-assisted path transmit the same information simultaneously at the same data rate. The propagation channels are modeled by taking into account propagation loss, Gamma–Gamma turbulence, and pointing error effects. At the receiver, the signals arriving through the direct path and the RIS-reflected path are coherently combined. To evaluate the effectiveness of this configuration, two diversity combining techniques, namely selection combining (SC) and maximum ratio combining (MRC), are investigated. Closed-form analytical expressions for the outage probability (P_{out}), average bit-error rate (BER), and ergodic capacity ($\overline{C}$) are derived using the probability density function (PDF), cumulative distribution function (CDF), and moment-generating function (MGF) of the end-to-end signal-to-noise ratio (SNR). The analysis indicates that jointly exploiting the DT and RIS-assisted links can provide noticeable performance gains by leveraging the complementary characteristics of the two propagation paths.

Keywords: optical wireless communication; reconfigurable intelligent surface (RIS); modulating retroreflector (MRR); selection combining (SC); maximum ratio combining (MRC); outage probability (P_{out}); average bit-error rate (BER); ergodic capacity ($\overline{C}$); Fox H-function

Academic Editor: Xizheng Ke

Received: 19 March 2026
Revised: 19 April 2026
Accepted: 24 April 2026
Published: 29 April 2026

1. Introduction

Underwater optical wireless communication (UOWC) is gaining increasing attention as a practical solution for high-speed underwater links, particularly in ocean exploration scenarios [1,2]. Unlike radio frequency (RF) and acoustic communication, which suffer from limited bandwidth, UOWC can support significantly higher data rates while maintaining secure and license-free operation [3]. In typical implementations, two similar transceivers communicate using narrow optical beams propagating through the water channel.

Despite the advantages of narrow laser beams, such as improved energy efficiency and reduced interception probability, they require accurate pointing, acquisition, and tracking (PAT) mechanisms at both transceivers [4]. These subsystems add considerable complexity, power consumption, and physical overhead, which limits the deployment of conventional UOWC systems, especially in harsh environments or on platforms with limited resources. A practical alternative is to adopt an asymmetric UOWC architecture, where one of the transceivers is replaced by an MRR-based terminal composed of a photodetector and a modulating retroreflector unit. Typically, the MRR integrates a light modulation mechanism with a passive retroreflecting structure [5]. The light modulators were developed using a number of methods, such as multiple quantum wells, micro-electromechanical systems, ferroelectric piezoelectric lead zirconate titanate thin films, and liquid crystals. The most common used retroreflectors are the corner cube reflector and cat's eye reflector [6]. The MRR may operate efficiently in a range of applications, such as communication with unmanned underwater vehicles (UUVs), because of its low-power modulators and small retroreflectors.

Because of the lack of a direct link and the presence of barriers that create dead zones for wireless communication, UOWC installation is not practicable for many applications [7]. Cooperative relaying has been intensively investigated to reduce the impact of channel limitations and enhance UOWC system performance [8]. RISs offer a simple and energy-efficient way to enhance signal propagation without relying on active relaying. Instead of performing complex processing, RIS structures adjust the characteristics of the incoming signal to guide it toward a desired direction [9,10]. These surfaces are usually implemented using planar metastructures composed of a large number of passive elements, supported by control circuitry that enables tuning of the amplitude, phase, and polarization of the reflected waves for improved signal quality and coverage [11].

1.1. Related Works

Numerous research studies have been presented in publications that focused on developing MRR devices [12], and practical MRR free-space optic (FSO) networks [13], providing a sufficient illustration of the viability of the MRR FSO technology. In [14], the link budget evaluation of MRR FSO systems in free space was first presented. A number of research studies have estimated statistics of the optical field moments in dual-pass transmission under turbulent circumstances [15]. The advantages of the RIS technique have recently been extensively studied for numerous types of wireless communication systems, including RF [16,17] and FSO [11,18]. A precise performance investigation for RIS-assisted wireless communication through general Fox H fading channels was provided by the authors in [19]. To combine an FSO connection over G–G turbulence and PE with an RIS-assisted RF link over Rayleigh fading, the authors in [20] investigated decode-and-forward relaying. Using RIS for linked autonomous vehicles and vehicular networks has recently been proposed [21,22], taking into account the advantages of traditional wireless communications. In [22], the authors investigated the average BER, P_{out}, and $\overline{C}$ of a mobile network with RIS enabled and random user movement. In [23], the effectiveness of multiple RIS-based vehicle communications was investigated using a double Generalized-gamma fading model.

Despite the growing interest in RIS-assisted UOWC systems, several limitations can still be observed in the existing literature. Most available studies focus on conventional RIS-UOWC links and do not consider the integration of MRR architectures. In addition, diversity combining techniques are rarely incorporated into these frameworks. In this work, we address these gaps by developing a unified model for RIS-assisted MRR-UOWC systems, where both the direct and RIS-assisted links are jointly considered. Furthermore,

exact closed-form expressions are derived using multivariate Fox H-functions, enabling a comprehensive evaluation of outage probability, BER, and ergodic capacity under realistic channel conditions. The inclusion of SC and MRC schemes within the same framework further distinguishes the proposed approach from existing studies.

To further highlight the differences between the proposed work and recent studies, a comparison is presented in Table 1.

Table 1. Comparison with recent RIS-assisted UOWC works.

Work	RIS	MRR	Channel Model	Analysis	Diversity
[24]	Yes	No	Turbulence + PE + Loss	Numerical/Approx.	No
[25]	Yes	No	Turbulence + PE	Partial closed-form	No
[10]	Yes	Yes	Turbulence + PE + Loss	Limited analysis	No
This Work	Yes	Yes	Turbulence + PE + Loss	Exact closed-form	SC, MRC

As shown in Table 1, existing works either consider RIS-assisted UOWC without MRR or MRR-based systems without a unified analytical framework. In contrast, the proposed work jointly incorporates RIS and MRR with exact closed-form analysis and diversity-combining techniques.

1.2. Motivations

Despite the growing interest in RIS-assisted UOWC systems, the performance benefits of diversity combining techniques in RIS-assisted MRR-UOWC links have not been thoroughly explored. In particular, the application of diversity schemes such as SC and MRC in this context has received limited attention in the existing literature.

Motivated by this gap, this paper presents a numerical performance analysis of an RIS-assisted MRR-UOWC system operating with intensity modulation and direct detection (IM/DD) over channels affected by propagation loss, G–G turbulence, and PE. Furthermore, the system performance is improved by exploiting diversity through the combination of signals reflected by RIS elements together with the DT from the source using SC and MRC schemes.

1.3. Contributions

The main contributions in this paper are: (i) We derive closed-form statistical formulas for the PDF, CDF, and MGF of the instantaneous electrical SNR γ_{DT} for the DT MRR UOWC link under the influence of G–G turbulence and PE with propagation loss. (ii) For the RIS-assisted MRR UOWC link, and under the same fading effects in (i), we derive closed-form statistical formulas of the PDF, CDF, and MGF of the instantaneous electrical SNR γ_{RIS} realized by the sum of products of independent but not identically distributed (i.ni.d) fading coefficients. (iii) By coherently combining received signals reflected by DT and RIS elements using the SC and MRC techniques, we derive closed-form statistical formulas of the PDF and CDF of the instantaneous electrical SNR (γ_{SC} and γ_{MRC}) under the same fading effects in (i). (iv) Using the derived PDF, CDF, and MGF of γ_{DT}, we evaluate the performance of the DT MRR UOWC link by developing a closed-form expression for the P_{out}, average BER of binary phase shift keying (BPSK) signals, and the $\overline{C}$ in terms of the multivariate Fox H-function (MFHF). (v) For comparison, using the derived PDF, CDF, and MGF of γ_{RIS}, we also perform an exact analysis of the previously mentioned performance quantities in terms of the MFHF for the RIS-assisted MRR UOWC link. (vi) Using the proved PDF and CDF of γ_{SC} and γ_{MRC}, we study the performance of both diversity techniques by deriving a closed-form expression for the same performance metrics in (iv) in terms of the MFHF. (vii) For the closed-form formulas of the P_{out}, average BER, and $\overline{C}$, derived in (iv) and (v),

numerical results are presented. The results indicate that employing the RIS-assisted link compared to the DT one enhances performance. Additionally, the performance is improved even further by the diversity approaches, specifically the SC and MRC techniques, with the MRC technique performing better than the SC technique.

1.4. Paper Organization

The upcoming sections of this paper are arranged as follows: Section 2 includes a detailed explanation of the system and channel models. Section 3 contains the statistical analysis of DT and RIS MRR UOWC links, followed by the statistical analysis of the received signals reflected by RIS elements and DT that are coherently combined using the SC and MRC techniques. Performance analysis through closed-form expressions for the P_{out}, average BER of BPSK signals, and the $\overline{C}$ is presented in Section 4. Section 5 contains the discussion of the numerical results. Finally, Section 6 provides the conclusion.

1.5. Notations

Main notations used in this paper are summarized in Table 2.

Table 2. List of main notations.

Symbol	Description	Symbol	Description
γ	Instantaneous SNR	γ_{DT}	SNR of direct link
γ_{RIS}	SNR of RIS-assisted link	γ_{SC}	SNR with selection combining
γ_{MRC}	SNR with maximal ratio combining	H_{DT}	Channel coefficient of direct link
H_{RIS}	Channel coefficient of RIS-assisted link	N	Number of RIS elements
z_d	Distance of direct link	z_1, z_2	Distances of RIS-assisted links
λ	Optical wavelength	$c(\lambda)$	Extinction coefficient
α, β	Gamma–Gamma turbulence parameters	ϵ	Pointing error parameter
A_o	PE fading coefficient at zero PE	$f_\gamma(\cdot)$	Probability density function
$F_\gamma(\cdot)$	Cumulative distribution function	$M_\gamma(\cdot)$	Moment generating function
$H_{p,q}^{m,n}(\cdot)$	Fox H-function	P_{out}	Outage probability
P_b	Bit-error rate	C	Ergodic capacity

2. System and Channel Models

We consider an underwater communication scenario involving two unmanned underwater vehicles (UUVs). The first vehicle (UUV1) is equipped with an optical transceiver, while the second vehicle (UUV2) employs a MRR unit, as illustrated in Figure 1. When a direct optical link is available, the transceiver emits an optical signal toward the MRR terminal. Upon reception, the MRR modulates the incoming light with the desired information and reflects it back toward the transceiver, where the signal is subsequently detected [26]. In practical underwater environments, obstacles such as marine objects may obstruct the direct path between the two vehicles. To mitigate this issue, a RIS consisting of N reflecting elements is deployed on a third UUV (UUV3). This RIS establishes line-of-sight (LOS) links with both the transceiver and the MRR unit, enabling an alternative communication path. In this configuration, the RIS intercepts the transmitted optical signal and redirects it toward the MRR terminal. After modulation, the reflected signal is again captured by the RIS and guided back toward the transceiver for final detection.

We assume that the RIS elements are spaced at half-wavelength intervals and experience i.ni.d channel conditions [27]. Under the assumption of perfect phase control at each RIS element, the received signal at the transceiver can be expressed as [17]:

$$y = s\sqrt{P_s}\left(H_{DT} + H_{RIS}\right) + n \tag{1}$$

where s is the sent signal with power P_s, H_{DT} is the channel fading caused by propagation loss, G–G turbulence, and PE in case of DT, and is given as $H_{DT} = h_{lDT}h_{fDT}h_{bDT}$, where h_{lDT} is the propagation loss component of DT MRR link, which is given as $h_{lDT} = \exp[-2c(\lambda)z_d]$, $c(\lambda)$ is the extinction coefficient, λ is the optical wavelength, and z_d is the distance between the transceiver and the MRR unit. We should note here that the heights of the transceiver and MRR unit are ignored to calculate the propagation loss for a direct link. h_{fDT} and h_{bDT} are the flat fading coefficients for the direct link between transceiver and MRR unit for the forward path (from the transceiver to the MRR unit) and the backward path (from the MRR unit to the transceiver), respectively.

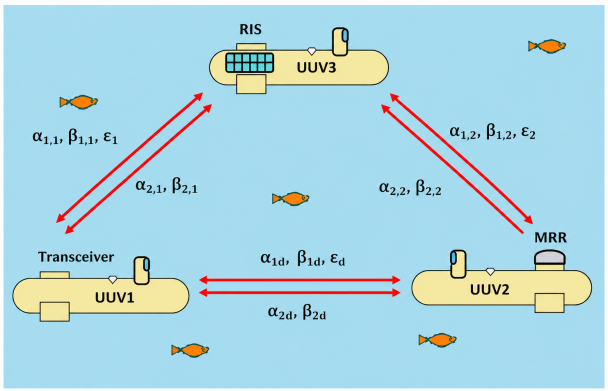

Figure 1. System model.

The channel coefficient of the RIS-assisted link, denoted by H_{RIS}, captures the joint impact of propagation attenuation, G–G turbulence, and PE effects. It can be expressed as $H_{RIS} = h_{lRIS}h_{fRIS}h_{bRIS}$, where h_{lRIS} represents the large-scale attenuation component of the cascaded RIS-assisted path. Specifically, the propagation loss is modeled as

$$h_{lRIS} = \exp\left[-2c(\lambda)\sum_{i=1}^{N}\sum_{j=1}^{2} z_{i,j}\right], \tag{2}$$

where N denotes the number of reflecting elements. The index $i \in \{1, 2, \ldots, N\}$ identifies each RIS element, while $j \in \{1, 2\}$ distinguishes the forward and backward propagation segments. In particular, $j = 1$ corresponds to the path between the transceiver and the ith RIS element, whereas $j = 2$ represents the path between the same RIS element and the MRR unit. To simplify the analytical treatment without sacrificing generality, all RIS elements are assumed to experience identical path lengths, such that $z_{i,1} = z_1$ and $z_{i,2} = z_2$ for all i. The small-scale fading contributions associated with the RIS-assisted link are modeled through the forward and backward components, denoted by h_{fRIS} and h_{bRIS}, respectively. These terms are constructed by aggregating the cascaded fading effects across all RIS elements as

$$h_{fRIS} = \sum_{i=1}^{N}\prod_{j=1}^{2} h_{fi,j}, \quad h_{bRIS} = \sum_{i=1}^{N}\prod_{j=1}^{2} h_{bi,j}, \tag{3}$$

where $h_{fi,j}$ and $h_{bi,j}$ correspond to the forward and backward fading coefficients associated with the ith RIS element along the jth propagation segment, and n is additive Gaussian noise with a mean of zero and a variance of σ_n^2.

G–G turbulence and PE are the two main signal degradation factors that affect both the DT and the RIS-assisted connections in addition to the path loss. The PDF of the G–G distribution, $f_{h_t}(h_t)$, is [28]:

$$f_{h_t}(h_t) = \frac{2(\alpha\beta)^{\frac{\alpha+\beta}{2}}}{\Gamma(\alpha)\Gamma(\beta)} h_t^{\frac{\alpha+\beta}{2}-1} \times K_{\alpha-\beta}\left(2\sqrt{\alpha\beta h_t}\right) \tag{4}$$

where h_t is the channel fading coefficient due to the G–G turbulence, α and β the parameters of fading related to the turbulence circumstances, $\Gamma(\cdot)$ is the gamma function, $K_x(\cdot)$ is the modified Bessel function of the second kind of order x, and $h_t > 0$. The PDF of the zero-boresight PE, $f_p(h_p)$, is [29]:

$$f_{hp}(h_p) = \frac{\epsilon^2}{{A_o}^{\epsilon^2}} {h_p}^{\epsilon^2-1} \tag{5}$$

where h_p is the channel fading coefficient due to the PE, A_o is the PE fading coefficient at zero PE, ϵ is the ratio between the equivalent beam radius at the destination and the PE displacement standard deviation (SD) at this destination, and $0 \leq h_p \leq A_o$. Although a generalized PE model could provide additional insights, the zero-boresight assumption is adopted in this work to maintain analytical tractability while preserving the essential system behavior. This assumption is widely used in the literature and enables closed-form derivations without excessive mathematical complexity. Moreover, prior studies have shown that nonzero boresight displacement and unequal jitter conditions introduce only marginal performance deviations [30], and thus do not fundamentally alter the observed system trends.

3. Closed-Form Statistical Analysis

In this section, we develop the PDF, CDF, and MGF of the instantaneous electrical end-to-end SNR of each of the DT (Section 3.1) and the RIS-assisted MRR links (Section 3.2). To improve the performance of the system model, we investigate two different diversity techniques between the aforementioned links, namely, the SC technique (Section 3.3.1) and the MRC technique (Section 3.3.2), by deriving the PDF and CDF of the instantaneous electrical end-to-end SNR of each.

3.1. DT MRR UOWC Link

The PDF, CDF, and MGF of the end-to-end SNR γ_{DT} of the DT MRR link are developed in this subsection. The forward path's channel fading is a union of G–G turbulence and PE, whereas the channel fading of the backward path is just turbulence. Because the MRR is made up of a retroreflector that reflects the light such that the pathways of the reflected rays and the incident rays are parallel, there is alignment in the backward direction. Hence, $h_{fDT} = h_{t1d}h_p$, and $h_{bDT} = h_{t2d}$, where h_{t1d} and h_{t2d} are the G–G turbulence channel fading coefficients for the forward and backward paths in the DT, respectively. To derive the statistical characterization of the received SNR, we start from the obtained channel model and proceed as follows. The PDF of the forward path's channel fading of the DT MRR link, h_{fDT}, is given as [26]:

$$f_{h_{fDT}}(x) = \frac{\alpha_{1d}\beta_{1d}{\epsilon_d}^2}{A_o\Gamma(\alpha_{1d})\Gamma(\beta_{1d})} G_{1,3}^{3,0}\left(\frac{\alpha_{1d}\beta_{1d}}{A_o}x \middle|_{{\epsilon_d}^2-1,\alpha_{1d}-1,\beta_{1d}-1}^{{\epsilon_d}^2}\right) \tag{6}$$

where α_{1d} and β_{1d} are the large-scale and small-scale parameters of the forward path of the direct link between the transceiver and the MRR unit, respectively. ϵ_d is the ratio between the equivalent beam radius at the transceiver and the PE displacement SD at the transceiver

of the forward path of the direct link between the transceiver and the MRR unit and $G_{\cdot,\cdot}^{\cdot,\cdot}(\cdot)$ is the Meijer's G-function defined in [31]. The PDF of the backward path's channel fading of the DT MRR link, h_{bDT}, is given as [26]:

$$f_{h_{bDT}}(x) = \frac{2(\alpha_{2d}\beta_{2d})^{\frac{\alpha_{2d}+\beta_{2d}}{2}}}{\Gamma(\alpha_{2d})\Gamma(\beta_{2d})} x^{\frac{\alpha_{2d}+\beta_{2d}}{2}-1} K_{\alpha_{2d}-\beta_{2d}}\left(2\sqrt{\alpha_{2d}\beta_{2d}x}\right) \tag{7}$$

where α_{2d} and β_{2d} are the large-scale and small-scale parameters of the backward path of the direct link between the transceiver and the MRR unit, respectively. The PDF of the composite channel fading of the DT MRR link H_{DT} is given as [26]:

$$f_{H_{DT}}(x) = \frac{\nu_d}{x} \times G_{1,5}^{5,0}\left(\frac{\rho_d x}{h_{l_{DT}}}\middle|_{\epsilon_d{}^2,\alpha_{1d},\beta_{1d},\alpha_{2d},\beta_{2d}}^{\epsilon_d{}^2+1}\right) \tag{8}$$

where $\nu_d = \epsilon_d{}^2/\{(\Gamma(\alpha_{1d})\Gamma(\beta_{1d}))\Gamma(\alpha_{2d})\Gamma(\beta_{2d})\}$, and $\rho_d = \{\alpha_{1d}\beta_{1d}\alpha_{2d}\beta_{2d}\}/A_o$. For IM/DD, after random variable (RV) transformation, the PDF of $\gamma_{DT} = H_{DT}^2\overline{\gamma}_{DT}$, where $\overline{\gamma}_{DT}$ is the average SNR of the DT MRR link, is calculated from the PDF of the composite channel fading as

$$f_\gamma(\gamma) = \frac{1}{2\sqrt{\gamma\overline{\gamma}}} f_H\left(\sqrt{\frac{\gamma}{\overline{\gamma}}}\right) \tag{9}$$

Substituting from (8) in (9), we get:

$$f_{\gamma_{DT}}(\gamma_{DT}) = \frac{\nu_d}{2\gamma_{DT}} \times H_{1,5}^{5,0}\left(\frac{\rho_d}{h_{l_{DT}}}\sqrt{\frac{\gamma_{DT}}{\overline{\gamma}_{DT}}}\middle|_{\psi_d}^{(\epsilon_d{}^2+1,1)}\right) \tag{10}$$

where $H_{\cdot,\cdot}^{\cdot,\cdot}(\cdot)$ is the Fox H-function defined in [32], and $\psi_d = \{(\epsilon_d{}^2,1),(\alpha_{1d},1),(\beta_{1d},1),(\alpha_{2d},1),(\beta_{2d},1)\}$. Based on the derived PDF expression, the corresponding CDF can be obtained through direct integration as follows:

$$F_\gamma(\gamma) = \int_0^\gamma f_\gamma(x)dx \tag{11}$$

Substituting for (10) in (11), we obtain

$$F_{\gamma_{DT}}(\gamma_{DT}) = \nu_d \times H_{2,6}^{5,1}\left(\frac{\rho_d}{h_{l_{DT}}}\sqrt{\frac{\gamma_{DT}}{\overline{\gamma}_{DT}}}\middle|_{\psi_d,(0,1)}^{(1,1),(\epsilon_d{}^2+1,1)}\right) \tag{12}$$

By applying standard integral transformations, the result in (12) can be directly expressed as

$$M_{\gamma_{DT}}(s) = \frac{\nu_d}{2} \times H_{2,5}^{5,1}\left(\frac{\rho_d}{h_{l_{DT}}\sqrt{s\overline{\gamma}_{DT}}}\middle|_{\psi_d}^{(\epsilon_d{}^2+1,1),(1,0.5)}\right) \tag{13}$$

3.2. RIS-Assisted MRR UOWC Link

In this subsection, we develop the closed-form formulas for the PDF, CDF, and MGF of the end-to-end SNR γ_{RIS} of the RIS-assisted MRR link. First, using Mellin transform, we find the PDF of each of the product of two i.ni.d RVs of the forward path h_{f_i} and that of the backward path h_{b_i}. Next, for N-RIS elements, we develop statistical results of the PDF of the channel fading of the forward path h_{fRIS} and that for the backward path h_{bRIS}. After that, we derive the combined PDF of the composite channel fading of the RIS-assisted MRR link H_{RIS}. Finally, using RV transformation we get the PDF and CDF of the instantaneous electrical SNR $\gamma_{RIS} = H_{RIS}^2\overline{\gamma}_{RIS}$, where $\overline{\gamma}_{RIS}$ is the average SNR of the RIS-assisted MRR link.

Although we can model the channel coefficients $h_{fi,1}$ and $h_{fi,2}$ to be similar, we consider a general assumption assuming fading coefficients $h_{fi,1}$ and $h_{fi,2}$ to be i.ni.d. Similarly, we consider $h_{bi,1}$ and $h_{bi,2}$ to be i.ni.d. Hence, $h_{fi,1} = h_{t1}h_{p1}$, $h_{fi,2} = h_{t2}h_{p2}$, $h_{bi,1} = h_{t1}$, and $h_{bi,2} = h_{t2}$ where $h_{fi,1}$ is the channel fading coefficient of the forward path between the transceiver and the ith element of the RIS module. $h_{fi,2}$ is the channel fading coefficient of the forward path between the ith element of the RIS module and the MRR unit. $h_{bi,1}$ is the channel fading coefficient of the backward path between the transceiver and the ith element of the RIS module, $h_{bi,2}$ is the channel fading coefficient of the backward path between the ith element of the RIS module and the MRR unit, h_{t1} and h_{t2} are the G–G turbulence channel fading coefficients in the forward path from the transceiver to the ith element of the RIS module, and from the ith element of the RIS module to the MRR unit, respectively, and h_{p1} and h_{p2} are the channel fading coefficients caused by the PE in the forward path from the transceiver to the ith element of the RIS module, and from the ith element of the RIS module to the MRR unit, respectively.

For the forward path, we apply the Mellin transform to obtain the PDF of $h_{fi} = \prod_{j=1}^{2} h_{fi,j} = h_{fi,1}h_{fi,2}$. Here, $h_{fi,1}$ and $h_{fi,2}$ are considered to be i.ni.d RVs distributed according to (4). Thus, the PDF of h_{fi} is given as:

$$f_{h_{fi}}(x) = \frac{1}{2\pi j}\frac{1}{x}\int_{\mathcal{L}}[h_{fi}^{r}]x^{-r}dr \tag{14}$$

where

$$[h_{fi}^{r}] = \prod_{j=1}^{2}[h_{fi,j}^{r}] = \prod_{j=1}^{2}\int_{0}^{\infty} u^{r} f_{h_{fi,j}}(u)du \tag{15}$$

is the rth moment of h_{fi}. Here, in the complex r-plane, $\mathcal{L}$ is an infinite contour with no singularities in the integrand in (14). In a manner similar to that used to derive Equation (6), $f_{h_{fi,j}}(x)$ is derived. The resulted expression is then substituted in (15) and using the identity ([31], eq.(07.34.21.0009.01)) to get the rth moment of h_{fi} as

$$[h_{fi}^{r}] = \prod_{j=1}^{2}\left\{\frac{\nu_{fj}}{{\rho_{fj}}^{r}} \times \frac{\Gamma(r+{\epsilon_j}^2)\Gamma(r+\alpha_{1,j})\Gamma(r+\beta_{1,j})}{\Gamma(r+{\epsilon_j}^2+1)}\right\} \tag{16}$$

where $\nu_{fj} = {\epsilon_j}^2/\{(\Gamma(\alpha_{1,j})\Gamma(\beta_{1,j}))\}$, and $\rho_{fj} = \{\alpha_{1,j}\beta_{1,j}\}/A_o$. $\alpha_{1,1}$ and $\beta_{1,1}$ are the large-scale and small-scale parameters of the forward path between the transceiver and the RIS module, respectively. $\alpha_{1,2}$ and $\beta_{1,2}$ are the large-scale and small-scale parameters of the forward path between the RIS module and the MRR unit, respectively. ϵ_1 is the ratio between the equivalent beam radius at the RIS module and the PE displacement SD at that module when the light is traveling from the transceiver to the RIS module, ϵ_2 is the ratio between the equivalent beam radius at the MRR unit and the PE displacement SD at the MRR when the light is traveling from the RIS module to the MRR unit. Substituting (16) in (14) and using Meijer's G-function definition to get the PDF of h_{fi} as

$$f_{h_{fi}}(x) = \frac{\prod_{j=1}^{2}\nu_{fj}}{x} \times G_{2,6}^{6,0}\left(x\prod_{j=1}^{2}\rho_{fj}\middle|\begin{matrix}\{{\epsilon_j}^2+1\}_{j=1}^{2} \\ \{{\epsilon_j}^2,\alpha_{1,j},\beta_{1,j}\}_{j=1}^{2}\end{matrix}\right) \tag{17}$$

For the backward path, to derive the PDF of h_{bi}, we use a similar manner to that used to derive $f_{h_{bi}}(x)$, where the rth moment of h_{bi} is derived as follows:

$$[h_{bi}^{r}] = \prod_{j=1}^{2}\left\{\frac{\nu_{bj}}{{\rho_{bj}}^{r}} \times \Gamma(r+\alpha_{2,j})\Gamma(r+\beta_{2,j})\right\} \tag{18}$$

where $\nu_{bj} = 1/\{\Gamma(\alpha_{2,j})\Gamma(\beta_{2,j})\}$, and $\rho_{bj} = \{\alpha_{2,j}\beta_{2,j}\}$, $\alpha_{2,2}$ and $\beta_{2,2}$ are the large-scale and small-scale parameters of the backward path between the MRR unit and the RIS module, respectively. $\alpha_{2,1}$ and $\beta_{2,1}$ are the large-scale and small-scale parameters of the backward path between the RIS module and the transceiver, respectively. Substituting (18) in (14) and using the definition of Meijer's G-function, we extract the PDF of h_{bi} as

$$f_{h_{bi}}(x) = \frac{\prod_{j=1}^{2} \nu_{bj}}{x} \times G_{0,4}^{4,0}\left(x \prod_{j=1}^{2} \rho_{bj} \Big|_{\{\alpha_{2,j},\beta_{2,j}\}_{j=1}^{2}}^{-} \right) \tag{19}$$

For N-RIS elements, the MGF of h_{fi} can be expressed as

$$M_{h_{fi}}(s) = \frac{1}{2\pi j} \prod_{j=1}^{2} \nu_{fj} {\rho_{fj}}^{r} \int_{\mathcal{L}} \left[\int_{0}^{\infty} e^{-sx} x^{r-1} dx \right] \times \prod_{j=1}^{2} \frac{\Gamma(r+{\epsilon_j}^2)\Gamma(r+\alpha_{1,j})\Gamma(r+\beta_{1,j})}{\Gamma(r+{\epsilon_j}^2+1)} dr \tag{20}$$

Solving the inner integral in (20) as

$$\int_{0}^{\infty} e^{-sx} x^{r-1} dx = s^{-r}\Gamma(r), \tag{21}$$

Substituting (21) in (20), and using the definition of Meijer's G-function, we get

$$M_{h_{fi}}(s) = \prod_{j=1}^{2} \nu_{fj} \times G_{3,6}^{6,1}\left(\frac{1}{s} \prod_{j=1}^{2} \rho_{fj} \Big|_{\{\epsilon_j^2,\alpha_{1,j},\beta_{1,j}\}_{j=1}^{2}}^{\{\epsilon_j^2+1\}_{j=1}^{2},1} \right) \tag{22}$$

Applying the inverse Laplace transform of the MGF, we find the PDF of h_{fRIS} as

$$f_{h_{fRIS}}(x) = \mathscr{L}^{-1}\left\{ \prod_{i=1}^{N} M_{h_{fi}}(s) \right\} \tag{23}$$

By substituting (22) in (23) and reversing the integration order, we obtain

$$\begin{aligned} f_{h_{fRIS}}(x) = \prod_{i=1}^{N}\prod_{j=1}^{2} \nu_{fi,j} \times \Bigg\{ \left(\frac{1}{2\pi j}\right)^{N} \int_{\mathcal{L}_i} \left(\prod_{j=1}^{2} \rho_{fi,j} \right)^{r_i} \times \prod_{j=1}^{2} \frac{\Gamma(r_i+{\epsilon_j}^2)\Gamma(r_i+\alpha_{1,j})\Gamma(r_i+\beta_{1,j})}{\Gamma(r_i+{\epsilon_j}^2+1)} \\ \times \left[\frac{1}{2\pi j} \int_{\mathcal{L}} \exp(sx) \times s^{-\sum_{i=1}^{N} r_i} ds \right] dr_i \Bigg\} \end{aligned} \tag{24}$$

where $\nu_{f1,1} = \nu_{f2,1} = \ldots = \nu_{fN,1}$, $\nu_{f1,2} = \nu_{f2,2} = \ldots = \nu_{fN,2}$, $\rho_{f1,1} = \rho_{f2,1} = \ldots = \rho_{fN,1}$, and $\rho_{f1,2} = \rho_{f2,2} = \ldots = \rho_{fN,2}$ to reduce the complexity of calculations. In the complex n_i-plane, $\mathcal{L}_i$ is an infinite contour with no singularities in the integrand in (24). The convergence conditions of multiple contour integrals describing MFHF are provided in [33]. Solving the inner integral in (24) as

$$\frac{1}{2\pi j} \int_{\mathcal{L}} \exp(sx) \times s^{-\sum_{i=1}^{N} r_i} ds = \frac{x^{-1+\sum_{i=1}^{N} r_i}}{\Gamma(\sum_{i=1}^{N} r_i)}, \tag{25}$$

Substituting (25) in (24) and using the N-MFHF definition in ([32], A.1), we obtain

$$f_{h_{fRIS}}(x) = \frac{\prod_{i=1}^{N}\prod_{j=1}^{2} \nu_{fi,j}}{x} \times H_{0,1:3,6;\ldots;3,6}^{0,0:6,1;\ldots;6,1}\left(\left\{ x \prod_{j=1}^{2} \rho_{fj} \right\}_1^N \Big|_{(1;\{1\}_1^N):\left\{\{(\epsilon_j^2,1),(\alpha_{1,j},1),(\beta_{1,j},1)\}_{j=1}^{2}\right\}_1^N}^{-:\left\{(1,1),\{(\epsilon_j^2+1,1)\}_{j=1}^{2}\right\}_1^N} \right) \tag{26}$$

For the backward path, to derive the PDF of $h_{bRIS} = \Sigma_{i=1}^{N} h_{bi}$, we use a similar manner to that used to derive h_{fRIS}, where

$$M_{h_{bi}}(s) = \frac{1}{2\pi j} \prod_{j=1}^{2} \nu_{bj} {\rho_{bj}}^{r} \int_{\mathcal{L}} \left[\int_{0}^{\infty} e^{-sx} x^{r-1} dx \right] \times \prod_{j=1}^{2} \left\{ \Gamma(r+\alpha_{2,j}) \Gamma(r+\beta_{2,j}) \right\} dr \tag{27}$$

Here, (27) has the same inner integral as that solved in (21). Substituting (21) in (27) and using the definition of Meijer's G-function, we obtain

$$M_{h_{bi}}(s) = \prod_{j=1}^{2} \nu_{bj} \times G_{1,4}^{4,1} \left(\frac{1}{s} \prod_{j=1}^{2} \rho_{bj} \Big|_{\{\alpha_{2,j}, \beta_{2,j}\}_{j=1}^{2}}^{1} \right) \tag{28}$$

Substituting (28) in (23) and interchanging the order of integration yields

$$\begin{aligned} f_{h_{bRIS}}(x) = \prod_{i=1}^{N} \prod_{j=1}^{2} \nu_{bi,j} \times \left\{ \left(\frac{1}{2\pi j} \right)^{N} \int_{\mathcal{L}_i} \left(\prod_{j=1}^{2} \rho_{bi,j} \right)^{r_i} \times \prod_{j=1}^{2} [\Gamma(r_i+\alpha_{2,j}) \Gamma(r_i+\beta_{2,j})] \right. \\ \left. \times \left[\frac{1}{2\pi j} \int_{\mathcal{L}} \exp(sx) \times s^{-\sum_{i=1}^{N} r_i} ds \right] dr_i \right\} \end{aligned} \tag{29}$$

where $\nu_{b1,1} = \nu_{b2,1} = \ldots = \nu_{bN,1}$, $\nu_{b1,2} = \nu_{b2,2} = \ldots = \nu_{bN,2}$, $\rho_{b1,1} = \rho_{b2,1} = \ldots = \rho_{bN,1}$ and $\rho_{b1,2} = \rho_{b2,2} = \ldots = \rho_{bN,2}$ for reducing the complexity of calculations. Substituting from (25) in (29), and using the N-MFHF definition in ([32], A.1), we obtain:

$$f_{h_{bRIS}}(x) = \frac{\prod_{i=1}^{N} \prod_{j=1}^{2} \nu_{bi,j}}{x} \times H_{0,1:1,4;\ldots;1,4}^{0,0:4,1;\ldots;4,1} \left(\left\{ x \prod_{j=1}^{2} \rho_{bj} \right\}_{1}^{N} \Big|_{(1;\{1\}_1^N):\left\{\{(\alpha_{2,j},1),(\beta_{2,j},1)\}_{j=1}^{2}\right\}_1^N}^{-:\{(1,1)\}_1^N} \right) \tag{30}$$

Using the PDFs for the forward and the backward paths derived in (26) and (30), the combined PDF of the composite channel fading of the RIS-assisted MRR link H_{RIS} is given as

$$f_{H_{RIS}}(H_{RIS}) = \int f_{H_{RIS}|h_{fRIS}}(H_{RIS}|h_{fRIS}) f_{h_{fRIS}}(h_{fRIS}) dh_{fRIS} \tag{31}$$

where $f_{H_{RIS}|h_{fRIS}}(H_{RIS}|h_{fRIS})$ is the conditional probability given $h_{f,RIS}$, which is derived to be:

$$f_{H_{RIS}|h_{fRIS}}(H_{RIS}|h_{fRIS}) = \prod_{i=1}^{N} \prod_{j=1}^{2} \nu_{bi,j} \times H_{0,1:1,4;\ldots;1,4}^{0,0:4,1;\ldots;4,1} \left(\left\{ \frac{H_{RIS}}{h_{fRIS}} \prod_{j=1}^{2} \rho_{bj} \right\}_{1}^{N} \Big|_{(1;\{1\}_1^N):\left\{\{(\alpha_{2,j},1),(\beta_{2,j},1)\}_{j=1}^{2}\right\}_1^N}^{-:\{(1,1)\}_1^N} \right) \tag{32}$$

Substituting (26) and (32) in (31) leads to:

$$f_{H_{RIS}}(H_{RIS}) = \frac{\prod_{i=1}^{N} \prod_{j=1}^{2} \nu_{ri,j}}{H_{RIS}} \times H_{0,2:4,10;\ldots;4,10}^{0,0:10,2;\ldots;10,2} \left(\left\{ \frac{H_{RIS}}{h_{lRIS}} \prod_{j=1}^{2} \rho_{j} \right\}_{1}^{N} \Big|_{(1;\{1\}_1^N),(1;\{1\}_1^N):\left\{\{\psi_{rj}\}_{j=1}^{2}\right\}_1^N}^{-:\left\{(1,1),(1,1),\{(\epsilon_j{}^2+1,1)\}_{j=1}^{2}\right\}_1^N} \right) \tag{33}$$

where $\psi_{rj} = \{(\epsilon_j{}^2, 1), (\alpha_{1,j}, 1), (\beta_{1,j}, 1), (\alpha_{2,j}, 1), (\beta_{2,j}, 1)\}$, $\nu_{ri,j} = \nu_{fi,j} \nu_{bi,j}$, and $\rho_{ri,j} = \rho_{fi,j} \rho_{bi,j}$. For IM/DD, and after RV transformation, the PDF of the instantaneous electrical SNR γ_{RIS} is derived to be

$$f_{\gamma_{RIS}}(\gamma_{RIS}) = \frac{\prod_{i=1}^{N} \prod_{j=1}^{2} \nu_{ri,j}}{2\gamma_{RIS}} \times H_{0,2:4,10;\ldots;4,10}^{0,0:10,2;\ldots;10,2} \left(\left\{ \frac{\prod_{j=1}^{2} \rho_{rj}}{h_{lRIS}} \sqrt{\frac{\gamma_{RIS}}{\overline{\gamma}_{RIS}}} \right\}_{1}^{N} \Big|_{(1;\{1\}_1^N),(1;\{1\}_1^N):\left\{\{\psi_{r,j}\}_{j=1}^{2}\right\}_1^N}^{-:\left\{(1,1),(1,1),\{(\epsilon_j{}^2+1,1)\}_{j=1}^{2}\right\}_1^N} \right) \tag{34}$$

To calculate the CDF of SNR, we utilize equation (34) in (11) and expand N-MFHF in terms of Mellin-Barnes integrals to obtain

$$F_{\gamma_{RIS}}(\gamma_{RIS}) = \frac{\prod_{i=1}^{N}\prod_{j=1}^{2}\nu_{r_{i,j}}}{2h_{l_{RIS}}} \times \left(\frac{1}{2\pi j}\right)^{N} \times \prod_{i=1}^{N} \times \int_{0}^{\gamma_{RIS}}\int_{\mathcal{L}_i} \gamma_{RIS}^{-1} \frac{\prod_{i=1}^{N}\left\{\frac{A_i(\zeta_i)}{B_i(\zeta_i)} Z_i^{\zeta_i}\right\}}{h_{l,RIS}\left(\Gamma(\sum_{i=1}^{N}\zeta_i)\right)^{2}} d\zeta_i d\gamma_{RIS} \quad (35)$$

where $A_i(\zeta_i) = \prod_{j=1}^{2}[\Gamma(\epsilon_j{}^2 - \zeta_i)\Gamma(\alpha_{1,j} - \zeta_i)\Gamma(\beta_{1,j} - \zeta_i)\Gamma(\alpha_{2,j} - \zeta_i)\Gamma(\beta_{2,j} - \zeta_i)[\Gamma(\zeta_i)]^2]$, $B_i(\zeta_i) = \prod_{j=1}^{2}\Gamma(\epsilon_j{}^2 + 1 - \zeta_i)$, and $Z_i = \prod_{j=1}^{2}\rho_{r_{i,j}} \times \sqrt{\frac{\gamma_{RIS}}{\overline{\gamma}_{RIS}}}$. Solving the inner integral in (35), we get

$$\int_{0}^{\gamma_{RIS}} {\gamma_{RIS}}^{-1+\sum_{i=1}^{N}\zeta_i} d\gamma_{RIS} = 2 \times {\gamma_{RIS}}^{\frac{1}{2}\sum_{i=1}^{N}\zeta_i} \frac{\Gamma(\sum_{i=1}^{N}\zeta_i)}{\Gamma(1+\sum_{i=1}^{N}\zeta_i)} \quad (36)$$

Using (36) in (35) and using the N-MFHF definition in ([32], A.1), we obtain

$$F_{\gamma_{RIS}}(\gamma_{RIS}) = \prod_{i=1}^{N}\prod_{j=1}^{2}\nu_{r_{i,j}} \times H_{0,2:4,10;\ldots;4,10}^{0,0:10,2;\ldots;10,2}\left(\left\{\frac{\prod_{j=1}^{2}\rho_{r_j}}{h_{l_{RIS}}}\sqrt{\frac{\gamma_{RIS}}{\overline{\gamma}_{RIS}}}\right\}_1^N \Bigg|_{(1;\{1\}_1^N),(0;\{1\}_1^N):\left\{\{\psi_{r,j}\}_{j=1}^{2}\right\}_1^N}^{-:\left\{(1,1),(1,1),\{(\epsilon_j{}^2+1,1)\}_{j=1}^{2}\right\}_1^N}\right) \quad (37)$$

Hence, the MGF is obtained to be

$$M_{\gamma_{RIS}}(s) = \frac{\prod_{i=1}^{N}\prod_{j=1}^{2}\nu_{r_{i,j}}}{2h_{l_{RIS}}^{2}} \times \left(\frac{1}{2\pi j}\right)^{N} \times \prod_{i=1}^{N} \times \int_{0}^{\gamma_{RIS}}\int_{\mathcal{L}_i} \exp(-s\gamma_{RIS}) \frac{\prod_{i=1}^{N}\left\{\frac{A_i(\zeta_i)}{B_i(\zeta_i)} Z_i^{\zeta_i}\right\}}{\left(\Gamma(\sum_{i=1}^{N}\zeta_i)\right)^{2}\gamma_{RIS}} d\zeta_i d\gamma_{RIS} \quad (38)$$

Solving the inner integral in (38) as

$$\int_{0}^{\infty} \exp(-s\gamma_{RIS}){\gamma_{RIS}}^{-1+\sum_{i=1}^{N}\zeta_i} d\gamma_{RIS} = s^{-\frac{1}{2}\sum_{i=1}^{N}\zeta_i}\Gamma\left(\frac{1}{2}\sum_{i=1}^{N}\zeta_i\right), \quad (39)$$

using (39) in (38), and using the N-MFHF definition in ([32], A.1), we obtain

$$M_{\gamma_{RIS}}(s) = \frac{\prod_{i=1}^{N}\prod_{j=1}^{2}\nu_{r_{i,j}}}{2} \times H_{1,2:4,10;\ldots;4,10}^{0,1:10,2;\ldots;10,2}\left(\left\{\frac{\prod_{j=1}^{2}\rho_{r_j}}{h_{l_{RIS}}\sqrt{s\overline{\gamma}_{RIS}}}\right\}_1^N \Bigg|_{(1;\{1\}_1^N),(1;\{1\}_1^N):\left\{\{\psi_{r,j}\}_{j=1}^{2}\right\}_1^N}^{(1;\{0.5\}_1^N)::\left\{(1,1),(1,1),\{(\epsilon_j{}^2+1,1)\}_{j=1}^{2}\right\}_1^N}\right) \quad (40)$$

3.3. Diversity Techniques Between DT and RIS-Assisted MRR Links

In this section, we focus on combining the received signals in a way that reduces the impact of channel fading and improves the reliability of the overall system. The studied diversity techniques are: SC technique (Section 3.3.1) and MRC technique (Section 3.3.2).

3.3.1. SC Technique

The most fundamental combining approach is the diversity SC technique. The SC evaluates the electrical SNR of each connection and picks the signal with the greatest SNR value. Thus, the selection combiner's SNR may be represented as $\gamma_{SC} = \max(\gamma_{DT}, \gamma_{RIS})$. When SC is applied at the destination for received signals from DT and RIS, the PDF and CDF of the resultant SNR γ_{SC} are as follows:

$$f_{\gamma_{SC}}(\gamma_{SC}) = \int_{0}^{\gamma_{SC}} f_{\gamma_{SC}}(\gamma_{DT}, \gamma_{RIS}) d\gamma_{DL} + \int_{0}^{\gamma_{SC}} f_{\gamma_{SC}}(\gamma_{DT}, \gamma_{RIS}) d\gamma_{RIS} \quad (41)$$

where $f_{\gamma_{SC}}(\gamma_{DT})$ is the joint PDF of the DT and the RIS-assisted MRR links, which are assumed to be i.ni.d, and hence $f_{\gamma_{SC}}(\gamma_{DT}, \gamma_{RIS}) = f_{\gamma_{DT}}(\gamma_{DT}) f_{\gamma_{RIS}}(\gamma_{RIS})$. Now, we expand the definition of MFHF and interchange the order of integration to get

$$f_{\gamma_{SC}}(\gamma_{SC}) = \frac{\nu_d \times \prod_{i=1}^{N}\prod_{j=1}^{2}\nu_{ri,j}}{2h_{l_{DT}}h_{l_{RIS}}}\left(\frac{1}{2\pi j}\right)^{N+1}\int_0^{\gamma_{RIS}}\gamma_{RIS}^{-2}\times\int_{\mathcal{L}}\frac{A_d(\zeta_d)}{B_d(\zeta_d)}{Y_d}^{\zeta_d}d\zeta_d d\gamma_{DT} \times\prod_{i=1}^{N}\int_{\mathcal{L}_i}\frac{\prod_{i=1}^{N}\left\{\frac{A_i(\zeta_i)}{B_i(\zeta_i)}{Z_i}^{\zeta_i}\right\}}{\left(\Gamma(\sum_{i=1}^{N}\zeta_i)\right)^2}d\zeta_i d\gamma_{RIS} \tag{42}$$

where $A_d(\zeta_d) = [\Gamma({\epsilon_d}^2-\zeta_d)\Gamma(\alpha_{1d}-\zeta_d)\Gamma(\beta_{1d}-\zeta_d)\Gamma(\alpha_{2d}-\zeta_d)\Gamma(\beta_{2d}-\zeta_d)]$, $B_d(\zeta_d) = \Gamma({\epsilon_d}^2+1-\zeta_d)$, and $Y_d = \rho_d \times \sqrt{\frac{\gamma_{DT}}{\overline{\gamma}_{DT}}}$. Next, we solve the inner integral in (42) to get

$$\int_0^{\gamma_{SC}}{\gamma_{SC}}^{-2+\frac{\zeta_d}{2}+\sum_{i=1}^{N}\zeta_i}d\gamma_{SC} = \frac{{\gamma_{SC}}^{\frac{\zeta_d}{2}-1+\frac{1}{2}\sum_{i=1}^{N}\zeta_i}\Gamma\left(\frac{\zeta_d}{2}-1+\frac{1}{2}\sum_{i=1}^{N}\zeta_i\right)}{\Gamma\left(\frac{\zeta_d}{2}+\frac{1}{2}\sum_{i=1}^{N}\zeta_i\right)} \tag{43}$$

Finally, we use the N-MFHF definition in ([32], A.1) to obtain

$$f_{\gamma_{SC}}(\gamma_{SC}) = \frac{\nu_d \times \prod_{i=1}^{N}\prod_{j=1}^{2}\nu_{ri,j}}{2\gamma_{SC}} \times H_{1,3:4,10;\ldots;4,10;1,5}^{0,1:10,2;\ldots;10,2;5,0}\left(\left\{\frac{\prod_{j=1}^{2}\rho_{rj}}{h_{l_{RIS}}}\sqrt{\frac{\gamma_{SC}}{\overline{\gamma}_{RIS}}}\right\}_1^N, \frac{\rho_d}{h_{l_{DT}}}\sqrt{\frac{\gamma_{SC}}{\overline{\gamma}_{DT}}}\middle|\begin{matrix}(2;\{0.5\}_1^N,0.5):\psi_1\\ \Psi_x,\Psi_x,(1;\{0.5\}_1^N,0.5):\psi_2\end{matrix}\right) \tag{44}$$

where $\Psi_1=\left\{\left\{(1,1),(1,1),({\epsilon_j}^2+1,1)_{j=1}^2\right\}_1^N,({\epsilon_d}^2+1,1)\right\}$, $\Psi_x=\left\{(1;\{1\}_1^N,0)\right\}$, and $\Psi_2=\left\{\left\{\{\psi_{r,j}\}_{j=1}^2\right\}_1^N,\psi_d\right\}$. To compute the CDF of SNR, we substitute (44) in (11) and expand N-MFHF in terms of Mellin–Barnes integrals to get:

$$F_{\gamma_{SC}}(\gamma_{SC}) = \frac{\nu_d \times \prod_{i=1}^{N}\prod_{j=1}^{2}\nu_{ri,j}}{2h_{l_{DT}}h_{l_{RIS}}}\left(\frac{1}{2\pi j}\right)^{N+1}\int_0^{\gamma_{SC}}\gamma_{SC}^{-1}\times\int_{\mathcal{L}}\frac{A_d(\zeta_d)}{B_d(\zeta_d)}{Y_d}^{\zeta_d}d\zeta_d\times\prod_{i=1}^{N}\int_{\mathcal{L}_i}\prod_{i=1}^{N}\left\{\frac{A_i(\zeta_i)}{B_i(\zeta_i)}{Z_i}^{\zeta_i}\right\} \times\frac{\Gamma(-1+\frac{\zeta_d}{2}+\frac{1}{2}\sum_{i=1}^{N}\zeta_i)}{[\Gamma(\sum_{i=1}^{N}\zeta_i)]^2\Gamma(\frac{1}{2}\sum_{i=1}^{N}\zeta_i+\frac{\zeta_d}{2})}d\zeta_i d\gamma_{SC} \tag{45}$$

Solving the inner integral in (45), we obtain

$$\int_0^{\gamma_{SC}}{\gamma_{SC}}^{-1+\frac{\zeta_d}{2}+\sum_{i=1}^{N}\zeta_i}d\gamma_{SC} = {\gamma_{SC}}^{\frac{\zeta_d}{2}-1+\frac{1}{2}\sum_{i=1}^{N}\zeta_i}\frac{\Gamma\left(\frac{\zeta_d}{2}+\frac{1}{2}\sum_{i=1}^{N}\zeta_i\right)}{\Gamma\left(\frac{\zeta_d}{2}+1+\frac{1}{2}\sum_{i=1}^{N}\zeta_i\right)} \tag{46}$$

Finally, we use the N-MFHF definition in ([32], A.1) to obtain

$$F_{\gamma_{SC}}(\gamma_{SC}) = \frac{\nu_d \times \prod_{i=1}^{N}\prod_{j=1}^{2}\nu_{ri,j}}{2} \times H_{1,3:4,10;\ldots;4,10;1,5}^{0,1:10,2;\ldots;10,2;5,0}\left(\left\{\frac{\prod_{j=1}^{2}\rho_{rj}}{h_{l_{RIS}}}\sqrt{\frac{\gamma_{SC}}{\overline{\gamma}_{RIS}}}\right\}_1^N, \frac{\rho_d}{h_{l_{DT}}}\sqrt{\frac{\gamma_{SC}}{\overline{\gamma}_{DT}}}\middle|\begin{matrix}(2;\{0.5\}_1^N,0.5):\psi_1\\ \Psi_x,\Psi_x,(0;\{0.5\}_1^N,0.5):\psi_2\end{matrix}\right) \tag{47}$$

3.3.2. MRC Technique

In the SC formulation above, we select the connection with the highest SNR. This is definitely not the best option because only one connection is considered while the other

is disregarded. The weights that maximize the output SNR are obtained via MRC, i.e., $\gamma_{MRC} = \gamma_{DT} + \gamma_{RIS}$. We compute the PDF and CDF of the resultant SNR γ_{MRC} by applying MRC at the destination for the received signals from DT and RIS as follows:

$$f_{\gamma_{MRC}}(\gamma_{MRC}) = \mathscr{L}^{-1}\{M_{\gamma_{tot.}}(s)\} \tag{48}$$

where $M_{\gamma_{tot.}}(s)$ is the product of the MGFs of the end-to-end SNR of DT and the RIS-assisted MRR links, which is derived to be

$$M_{\gamma_{tot.}} = \frac{\nu_d \times \prod_{i=1}^{N}\prod_{j=1}^{2}\nu_{ri,j}}{4} \times H_{1,2:4,10;\ldots;4,10;2,5}^{0,1:10,2;\ldots;10,2;5,1}\left(\left\{\frac{\prod_{j=1}^{2}\rho_{rj}}{h_{l_{RIS}}}\sqrt{\frac{1}{s\overline{\gamma}_{RIS}}}\right\}_1^N, \left\{\frac{\rho_d}{h_{l_{DT}}}\sqrt{\frac{1}{s\overline{\gamma}_{DT}}}\right\}\Bigg|_{\Psi_x,\Psi_x:\Psi_2}^{(1;\{0.5\}_1^N,0):\Psi_1,(1,0.5)}\right) \tag{49}$$

Substituting (49) in (48) and interchanging the order of integration to get an inner integral that can be solved as

$$\frac{1}{2\pi j}\int_{\mathcal{L}} \exp(s\gamma_{MRC}) s^{-\frac{1}{2}\sum_{i=1}^{N}(\zeta_d-\zeta_i)} = \frac{\gamma_{MRC}^{\sum_{i=1}^{N}\frac{\zeta_d}{2}-\frac{\zeta_i}{2}-1}}{\Gamma\left(\frac{\zeta_d}{2}+\sum_{i=1}^{N}\frac{\zeta_i}{2}\right)} \tag{50}$$

Finally, we use the N-MFHF definition in ([32], A.1) to obtain

$$\begin{aligned} f_{\gamma_{MRC}}(\gamma_{MRC}) = {} & \frac{\nu_d \times \prod_{i=1}^{N}\prod_{j=1}^{2}\nu_{ri,j}}{4\gamma_{MRC}} \times H_{1,3:4,10;\ldots;4,10;2,5}^{0,1:10,2;\ldots;10,2;5,1} \\ & \left(\left\{\frac{\prod_{j=1}^{2}\rho_{rj}}{h_{l_{RIS}}}\sqrt{\frac{\gamma_{MRC}}{\overline{\gamma}_{RIS}}}\right\}_1^N, \frac{\rho_d}{h_{l_{DT}}}\sqrt{\frac{\gamma_{MRC}}{\overline{\gamma}_{DT}}}\Bigg|_{\Psi_x,\Psi_x,(1;\{0.5\}_1^N,0.5):\Psi_2}^{(1;\{0.5\}_1^N,0):\psi_1,(1,0.5)}\right) \end{aligned} \tag{51}$$

To compute the CDF of SNR, we use a similar manner to that used in deriving (47):

$$\begin{aligned} F_{\gamma_{MRC}}(\gamma_{MRC}) = {} & \frac{\nu_d \times \prod_{i=1}^{N}\prod_{j=1}^{2}\nu_{ri,j}}{4} \times H_{1,3:4,10;\ldots;4,10;2,5}^{0,1:10,2;\ldots;10,2;5,1} \\ & \left(\left\{\frac{\prod_{j=1}^{2}\rho_{rj}}{h_{l_{RIS}}}\sqrt{\frac{\gamma_{MRC}}{\overline{\gamma}_{RIS}}}\right\}_1^N, \frac{\rho_d}{h_{l_{DT}}}\sqrt{\frac{\gamma_{MRC}}{\overline{\gamma}_{DT}}}\Bigg|_{\Psi_x,\Psi_x,(0;\{0.5\}_1^N,0.5):\Psi_2}^{(1;\{0.5\}_1^N,0):\psi_1,(1,0.5)}\right) \end{aligned} \tag{52}$$

4. Performance Analysis

In this section, the performance of the considered DT and RIS-assisted MRR-UOWC links is analyzed using the statistical expressions derived in the previous section. In Section 4.1, the P_{out} is derived to evaluate the reliability of the system. In Section 4.2, the average BER for BPSK modulation is obtained. Finally, in Section 4.3, the $\overline{C}$ is derived to characterize the achievable data rate of the considered system. The analytical results are expressed in terms of the MFHF, enabling efficient numerical evaluation under the combined effects of G–G turbulence, PE, and propagation loss.

4.1. Outage Probability

Outage probability quantifies the effect of fading in a communication system. It is technically defined as the likelihood of SNR falling lower than a particular threshold value γ_{th}. The following is an exact equation for the outage probability:

$$P_{out} = Pr(\gamma \leq \gamma_{th}) = F_{\gamma}(\gamma_{th}) \tag{53}$$

Hence, using Equations (12), (35), (47) and (52) in (53), we get the outage probabilities of the DT MRR link, RIS-assisted MRR link, SC, and MRC, respectively.

4.2. Average BER

The average BER is used to assess the data transfers reliability. The average BER for binary modulations using the CDF of SNR is provided as:

$$\overline{P}_b = \frac{q^p}{2\Gamma(p)} \int_0^\infty \gamma^{p-1} \exp(-q\gamma) F_\gamma(\gamma) d\gamma \tag{54}$$

where p and q are specific parameters of modulation. To derive an expression for the average BER of the DT MRR link, we substitute the CDF of the DT link of (12) in (54), apply the definition of Fox H-function, and reverse the integration order to obtain

$$\overline{P}_{b,DT} = \frac{q^p \nu_d}{2h_{lDT}\Gamma(p)} \times \frac{1}{2\pi j} \int_0^\infty {\gamma_{DT}}^{p-1} \exp(-q\gamma_{DT}) \times \frac{A_d(\zeta_d)\Gamma(\zeta_d)}{B_d(\zeta_d)\Gamma(1+\zeta_d)} \times \Upsilon_d^{\zeta_d} d\zeta_d d\gamma_{DT} \tag{55}$$

Solving the inner integral in (55), we obtain

$$\int_0^\infty {\gamma_{DT}}^{p-1+\frac{\zeta_d}{2}} exp(-q\gamma_{DL}) d\gamma_{DT} = \left(\frac{1}{q}\right)^{p+\frac{\zeta_d}{2}} \Gamma\left(p + \frac{\zeta_d}{2}\right) \tag{56}$$

Finally, we use the definition of Fox H-function to obtain

$$\overline{P}_{b,DT} = \frac{\nu_d}{2\Gamma(p)} \times H_{3,6}^{5,2}\left(\frac{\rho_d}{h_{lDT}\sqrt{q\overline{\gamma}_{DT}}} \middle|^{(1,1),(\epsilon_d{}^2+1,1),(1-p,0.5)}_{\Psi_d,(0,1)} \right) \tag{57}$$

To derive an expression for the average BER of the RIS-assisted MRR link, we substitute the CDF of the RIS link of (37) in (54), apply the definition of MFHF, and reverse the integration order to get

$$\begin{aligned} \overline{P}_{b,RIS} = {} & \frac{q^p \prod_{i=1}^N \prod_{j=1}^2 \nu_{ri,j}}{2\Gamma(p) h_{lRIS}} \times \left(\frac{1}{2\pi j}\right)^N \int_0^\infty {\gamma_{RIS}}^{p-1} \exp(-q\gamma_{RIS}) \\ & \prod_{i=1}^N \int_{\mathcal{L}_i} \frac{A_i(\zeta_i) Z_i^{\zeta_i} \Gamma(\sum_{i=1}^N \zeta_i)}{B_i(\zeta_i)\Gamma(\sum_{i=1}^N \zeta_i)\Gamma(\sum_{i=1}^N \zeta_i)\Gamma(1+\sum_{i=1}^N \zeta_i)} d\zeta_i d\gamma_{RIS} \end{aligned} \tag{58}$$

Solving the inner integral in (58), we have

$$\int_0^\infty {\gamma_{RIS}}^{p-1+\frac{1}{2}\sum_{i=1}^N \zeta_i} \exp(-q\gamma_{RIS}) d\gamma_{RIS} = \left(\frac{1}{q}\right)^{p+\frac{1}{2}\sum_{i=1}^N \zeta_i} \Gamma\left(p + \frac{1}{2}\sum_{i=1}^N \zeta_i\right) \tag{59}$$

Finally, we use the N-MFHF definition in ([32], A.1) to obtain

$$\begin{aligned} \overline{P}_{b,RIS} = {} & \frac{\prod_{i=1}^N \prod_{j=1}^2 \nu_{ri,j}}{2\Gamma(p)} \times H_{1,2:L+2,5L;\ldots;L+2,5L}^{0,2:5L,2;\ldots;5L,2} \\ & \left(\left\{ \frac{\prod_{j=1}^2 \rho_{r_j}}{h_{lRIS}\sqrt{q\overline{\gamma}_{RIS}}} \right\}_1^N \middle|^{(1-p;\{0.5\}_1^N):\left\{(1,1),(1,1),\{(\epsilon_j{}^2+1,1)\}_{j=1}^2\right\}_1^N}_{(1;\{1\}_1^N),(0;\{1\}_1^N):\left\{\{\psi_{r,j}\}_{j=1}^2\right\}_1^N} \right) \end{aligned} \tag{60}$$

To derive the average BER of the SC, we substitute the CDF of (47) in (54), apply the definition of MFHF, and reverse the order of integration to obtain

$$\begin{aligned} \overline{P}_{b,SC} = {} & \frac{q^p \left(\nu_d \times \prod_{i=1}^N \prod_{j=1}^2 \nu_{ri,j}\right)}{4\Gamma(p) h_{lDT} h_{lRIS}} \left(\frac{1}{2\pi j}\right)^{N+1} \int_0^\infty \gamma_{SC}^{p-1} e^{-q\gamma_{SC}} \prod_{i=1}^N \int_{\mathcal{L}_i} \frac{\Gamma\left(-1+\frac{\zeta_d}{2}+\frac{1}{2}\sum_{i=1}^N \zeta_i\right)}{\left(\Gamma(\sum_{i=1}^N \zeta_i)\right)^2 \Gamma\left(1+\frac{\zeta_d}{2}+\frac{1}{2}\sum_{i=1}^N \zeta_i\right)} \\ & \times \frac{A_d(\zeta_d)\Gamma(\zeta_d)}{B_d(\zeta_d)\Gamma(1+\zeta_d)} \Upsilon_d^{\zeta_d} \prod_{i=1}^N \left\{ \frac{A_i(\zeta_i)}{B_i(\zeta_i)} Z_i^{\zeta_i} \right\} d\zeta_d d\zeta_i d\gamma_{MRC} \end{aligned} \tag{61}$$

Solving the inner integral in (61), we have

$$\int_0^\infty {\gamma_{SC}}^{p-1+\frac{\zeta_d}{2}+\frac{1}{2}\sum_{i=1}^{N}\zeta_i}\exp(-q\gamma_{SC})d\gamma_{SC} = \left(\frac{1}{q}\right)^{p+\frac{\zeta_d}{2}+\frac{1}{2}\sum_{i=1}^{N}\zeta_i}\Gamma\left(p+\frac{\zeta_d}{2}+\frac{1}{2}\sum_{i=1}^{N}\zeta_i\right) \quad (62)$$

Finally, we use the *N*-MFHF definition in ([32], A.1) to obtain

$$\begin{aligned}\overline{P}_{b,SC} = {} & \frac{\nu_d\times\prod_{i=1}^{N}\prod_{j=1}^{2}\nu_{ri,j}}{4\Gamma(p)}\times H_{2,3:4,10;\ldots;4,10;1,5}^{0,2:10,2;\ldots;10,2;5,0} \\ & \left(\left\{\frac{\prod_{j=1}^{2}\rho_{rj}}{h_{lRIS}\sqrt{q\overline{\gamma}_{RIS}}}\right\}_1^N, \frac{\rho_d}{h_{lDT}\sqrt{q\overline{\gamma}_{DT}}}\middle|_{\Psi_x,\Psi_x,(0;\{0.5\}_1^N,0.5):\psi_2}^{(2;\{0.5\}_1^N,0.5),(1-p;\{0.5\}_1^N,0.5):\psi_1}\right)\end{aligned} \quad (63)$$

To derive the average BER of the MRC, we substitute the CDF of (52) in (54), apply the definition of MFHF, and interchange the integration order to get

$$\begin{aligned}\overline{P}_{b,MRC} = {} & \frac{q^p\left(\nu_d\times\prod_{i=1}^{N}\prod_{j=1}^{2}\nu_{ri,j}\right)}{8\Gamma(p)h_{l,DT}h_{l,RIS}}\left(\frac{1}{2\pi j}\right)^{N+1}\int_0^\infty\gamma_{MRC}^{p-1}e^{-q\gamma_{MRC}}\prod_{i=1}^{N}\int_{\mathcal{L}_i}\frac{\frac{1}{2}\Gamma\left(\sum_{i=1}^{N}\zeta_i\right)}{\Gamma\left(\sum_{i=1}^{N}\zeta_i\right)^2\Gamma\left(1+\frac{1}{2}\sum_{i=1}^{N}\zeta_i+\frac{\zeta_d}{2}\right)}d\zeta_d \\ & \times\frac{A_d(\zeta_d)\Gamma\left(\frac{\zeta_d}{2}\right)}{B_d(\zeta_d)}Y_d^{\zeta_d}\prod_{i=1}^{N}\left\{\frac{A_i(\zeta_i)}{B_i(\zeta_i)}Z_i^{\zeta_i}\right\}d\zeta_i\,d\gamma_{MRC}\end{aligned} \quad (64)$$

Next, we solve the inner integral which as we did in (62). Finally, we use the *N*-MFHF definition in ([32], A.1) to obtain

$$\begin{aligned}\overline{P}_{b,MRC} = {} & \frac{\nu_d\times\prod_{i=1}^{N}\prod_{j=1}^{2}\nu_{ri,j}}{8\Gamma(p)} \\ & \times H_{2,3:4,10;\ldots;4,10;2,5}^{0,2:10,2;\ldots;10,2;5,1}\left(\left\{\frac{\prod_{j=1}^{2}\rho_{rj}}{h_{lRIS}\sqrt{q\overline{\gamma}_{RIS}}}\right\}_1^N, \frac{\rho_d}{h_{lDT}\sqrt{q\overline{\gamma}_{DT}}}\middle|_{\psi_x,\psi_x,(0;\{0.5\}_1^N,0.5):\psi_2}^{(1;\{0.5\}_1^N,0),(1-p;\{0.5\}_1^N,0.5):\psi_1,(1,0.5)}\right)\end{aligned} \quad (65)$$

4.3. Ergodic Capacity

Assuming a Gaussian codebook at the channel input, the ergodic capacity is the highest transmission rate with an arbitrarily low error probability, which is provided as follows:

$$\overline{C} = +[\log_2(1+\frac{e}{2\pi}\gamma)] = \int_0^\infty\log_2\left(1+\frac{e}{2\pi}\gamma\right)f_\gamma(\gamma)d\gamma \quad (66)$$

To derive the ergodic capacity of the DT MRR link, we substitute the PDF of the DT link of (10) in (66), use the definition of Fox H-function, and reverse the integration order to obtain

$$\overline{C}_{DT} = \frac{\nu_d}{2\ln(2)h_{lDT}}\times\frac{1}{2\pi j}\int_0^\infty{\gamma_{DT}}^{-1}\ln\left(1+\frac{e}{2\pi}\gamma_{DT}\right)\times\frac{A_d(\zeta_d)\Gamma(\zeta_d)}{B_d(\zeta_d)\Gamma(1+\zeta_d)}\times Y_d^{\zeta_d}d\zeta_d d\gamma_{DT} \quad (67)$$

Applying the final-value theorem and solving the inner integral in (67), we obtain

$$\begin{aligned}&\int_0^\infty{\gamma_{DT}}^{-1+\frac{\zeta_d}{2}}\ln\left(1+\frac{e}{2\pi}\gamma_{DT}\right)d\gamma_{DT} \\ &\qquad = \frac{1}{2\pi j}\int_{\mathcal{L}}\frac{\Gamma(-u+1)\left(\Gamma(u)\right)^2}{\Gamma(u+1)}\left(\frac{e}{2\pi}\right)^u\left(\frac{1}{\delta}\right)^{u+\frac{\zeta_d}{2}}\Gamma\left(u+\frac{\zeta_d}{2}\right)du\end{aligned} \quad (68)$$

where δ is in the order 10^{-6}. Using the definition of Fox H-function in ([32], A.1) yields

$$\overline{C}_{DT} = \frac{v_d}{2\ln(2)}\times H_{1,0:1,5:1,1}^{0,1:5,0:1,1}\left(\left\{\frac{\rho_d}{h_{lDT}\sqrt{\delta\overline{\gamma}_{DT}}}\right\}, \frac{e}{2\pi\delta}\middle|_{-:\Psi_6}^{(1;0.5,1):\Psi_5}\right) \quad (69)$$

To derive the ergodic capacity of the RIS-assisted MRR link, we substitute the PDF of the RIS link of (34) in (66), use the definition of Fox H-function, and reverse the integration order to obtain

$$\overline{C}_{RIS} = \frac{\prod_{i=1}^{N}\prod_{j=1}^{2}\nu_{ri,j}}{2\ln(2)\,h_{lRIS}}\left(\frac{1}{2\pi j}\right)^{N}\int_{0}^{\infty}\gamma_{RIS}^{-1}\ln\left(1+\frac{e}{2\pi}\gamma_{DT}\right)\prod_{i=1}^{N}\int_{\mathcal{L}_i}\frac{A_i(\zeta_i)Z_i^{\zeta_i}}{B_i(\zeta_i)\Gamma\left(\sum_{i=1}^{N}\zeta_i\right)\Gamma\left(\sum_{i=1}^{N}\zeta_i\right)}\,d\zeta_i\times d\gamma_{RIS} \tag{70}$$

Solving the inner integral solution in (70), we obtain

$$\int_{0}^{\infty}\gamma_{RIS}{}^{-1+\frac{1}{2}\sum_{i=1}^{N}\zeta_i}\ln\left(1+\frac{e}{2\pi}\gamma_{RIS}\right)d\gamma_{RIS} = \frac{1}{2\pi j}\times\int_{\mathcal{L}}\frac{\Gamma(-u+1)(\Gamma(u))^2}{\Gamma(u+1)}\times\left(\frac{e}{2\pi}\gamma_{RIS}\right)^{u}du \tag{71}$$

Applying the final-value theorem and using the definition of N-MFHF in ([32], A.1), we get

$$\overline{C}_{RIS} = \frac{\prod_{i=1}^{N}\prod_{j=1}^{2}\nu_{ri,j}}{2\ln(2)}\times H_{1,2:4,10;\ldots;4,10;1,1}^{0,1:10,2;\ldots;10,2;1,1}\left(\left\{\frac{\prod_{j=1}^{2}\rho_{rj}}{h_{lRIS}\sqrt{\delta\overline{\gamma}_{RIS}}}\right\}_1^N,\frac{e}{2\pi\delta}\middle|\begin{matrix}(1;\{0.5\}_1^N,1):(1,1),\left\{(1,1),(1,1),\{(\epsilon_j{}^2+1,1)\}_{j=1}^{2}\right\}_1^N\\ \Psi_x,\Psi_x:\left\{\{\psi_{rj}\}_{j=1}^{2}\right\}_1^N,(0,1)\end{matrix}\right) \tag{72}$$

To derive the ergodic capacity of the SC, we substitute the PDF of (44) in (66), apply the definition of MFHF, and reverse the integration order to get

$$\begin{aligned}\overline{C}_{SC} = {}& \frac{\nu_d\times\prod_{i=1}^{N}\prod_{j=1}^{2}\nu_{ri,j}}{2\ln(2)\,h_{lDT}h_{lRIS}}\left(\frac{1}{2\pi j}\right)^{N+1}\int_{0}^{\infty}\gamma_{SC}^{-1}\ln\left(1+\tfrac{e}{2\pi}\gamma_{SC}\right)\prod_{i=1}^{N}\int_{\mathcal{L}_i}\frac{\Gamma\left(-1+\frac{\zeta_d}{2}+\frac{1}{2}\sum_{i=1}^{N}\zeta_i\right)}{\Gamma\left(\sum_{i=1}^{N}\zeta_i\right)^2\Gamma\left(1+\frac{\zeta_d}{2}+\frac{1}{2}\sum_{i=1}^{N}\zeta_i\right)}\,d\zeta_i\\ &\times\frac{A_d(\zeta_d)\Gamma\left(\frac{\zeta_d}{2}\right)}{B_d(\zeta_d)}\,\Upsilon_d^{\zeta_d}\prod_{i=1}^{N}\left\{\frac{A_i(\zeta_i)}{B_i(\zeta_i)}Z_i^{\zeta_i}\right\}d\zeta_d\,d\gamma_{SC}\end{aligned} \tag{73}$$

Solving the inner integral in (73) as

$$\begin{aligned}\int_{0}^{\infty}\gamma_{SC}{}^{-1+\frac{\zeta_d}{2}+\frac{1}{2}\sum_{i=1}^{N}\zeta_i}\ln\left(1+\frac{e}{2\pi}\gamma_{SC}\right)d\gamma_{SC} = {}& \frac{1}{2\pi j}\times\int_{\mathcal{L}}\frac{\Gamma(-u+1)(\Gamma(u))^2}{\Gamma(u+1)}\times\left(\frac{e}{2\pi}\right)^{u}\\ &\times\left(\frac{1}{\delta}\right)^{u+\frac{\zeta_d}{2}+\frac{1}{2}\sum_{i=1}^{N}\zeta_i}\Gamma\left(u+\frac{\zeta_d}{2}+\frac{1}{2}\sum_{i=1}^{N}\zeta_i\right)du\end{aligned} \tag{74}$$

Finally, we use the N-MFHF definition in ([32], A.1) to obtain

$$\overline{C}_{SC} = \frac{\nu_d\times\prod_{i=1}^{N}\prod_{j=1}^{2}\nu_{ri,j}}{2\ln(2)}\times H_{2,3:4,10;\ldots;4,10;1,5;1,1}^{0,2:10,2;\ldots;10,2;5,0;1,1}\left(\left\{\frac{\prod_{j=1}^{2}\rho_{rj}}{h_{l,RIS}\sqrt{\delta\overline{\gamma}_{RIS}}}\right\}_1^N,\frac{\rho_d}{h_{l,DT}\sqrt{\delta\overline{\gamma}_{DT}}},\frac{e}{2\pi\delta}\middle|\begin{matrix}\psi_3\\ \psi_4\end{matrix}\right) \tag{75}$$

where $\psi_3 = \{(2;\{0.5\}_1^N,0.5,0),(1;\{0.5\}_1^N,0.5,1):(1,1),\psi_1\}$, and $\psi_4 = \{(1;\{1\}_1^N,0,0),(1;\{1\}_1^N,0,0),(1;\{0.5\}_1^N,0.5,0):\psi_2,(0,1)\}$. To derive the ergodic capacity of the MRC, we substitute the PDF of (51) in (66), use the definition of Fox H-function, and reverse the integration order to get

$$\begin{aligned}\overline{C}_{MRC} = {}& \frac{\nu_d\times\prod_{i=1}^{N}\prod_{j=1}^{2}\nu_{ri,j}}{4\ln(2)\,h_{lDT}h_{lRIS}}\left(\frac{1}{2\pi j}\right)^{N+1}\int_{0}^{\infty}\gamma_{MRC}^{-1}\ln\left(1+\frac{e}{2\pi}\gamma_{MRC}\right)\\ &\prod_{i=1}^{N}\int_{\mathcal{L}_i}\frac{\frac{1}{2}\Gamma\left(\sum_{i=1}^{N}\zeta_i\right)}{\Gamma\left(\sum_{i=1}^{N}\zeta_i\right)^2\Gamma\left(1+\frac{1}{2}\sum_{i=1}^{N}\zeta_i+\frac{\zeta_d}{2}\right)}\,d\zeta_i\times\frac{A_d(\zeta_d)\Gamma\left(\frac{\zeta_d}{2}\right)}{B_d(\zeta_d)}\,\Upsilon_d^{\zeta_d}\prod_{i=1}^{N}\left\{\frac{A_i(\zeta_i)}{B_i(\zeta_i)}Z_i^{\zeta_i}\right\}d\zeta_d\,d\gamma_{MRC}\end{aligned} \tag{76}$$

Using the solution of the inner integral in (74) and applying the definition of N-MFHF in ([32], A.1), we obtain

$$\overline{C}_{MRC} = \frac{\nu_d\times\prod_{i=1}^{N}\prod_{j=1}^{2}\nu_{ri,j}}{4\ln(2)}\times H_{2,3:4,10;\ldots;4,10;2,5;1,1}^{0,2:10,2;\ldots;10,2;5,1;1,1}\left(\left\{\frac{\prod_{j=1}^{2}\rho_{rj}}{h_{lRIS}\sqrt{\delta\overline{\gamma}_{RIS}}}\right\}_1^N\frac{\rho_d}{h_{lDT}\sqrt{\delta\overline{\gamma}_{DT}}},\frac{e}{2\pi\delta}\middle|\begin{matrix}\psi_5\\ \psi_6\end{matrix}\right) \tag{77}$$

where $\psi_5 = \{(1;\{0.5\}_1^N,0,0),(1;\{0.5\}_1^N,0.5,1):(1,1),\psi_1,(1,0.5)\}$ and $\psi_6 = \{(1;\{1\}_1^N,0,0),(1;\{1\}_1^N,0,0),(1;\{0.5\}_1^N,0.5,0):\psi_2,(0,1)\}$.

5. Results and Discussion

In this section, we use numerical evaluations to compare the performance of DT and RIS-assisted MRR UOWC links utilizing the IM/DD detection technique under the combined influence of G–G water turbulence and PE over clear ocean and coastal ocean. Using the MFHF implementation in the MATLAB R2025b code [34], we evaluate the analytical expressions that have been derived. For DT, we assume a link distance of $z_d = 10$ m. Assuming that $z_1 = z_2 = z_d/2$, the optical RIS is positioned halfway between the transceiver and MRR unit. The used system parameters are as follows: $\lambda = 532$ nm, $\alpha_{1d} = 4.6151$, $\beta_{1d} = 2.2448$, $\alpha_{2d} = 4.6001$, $\beta_{2d} = 1.5233$, $\alpha_{1,1} = 3.7258$, $\beta_{1,1} = 3$, $\alpha_{2,1} = 3.5216$, $\beta_{2,1} = 1.5$, $\alpha_{1,2} = 3.4642$, $\beta_{1,2} = 2$, $\alpha_{2,2} = 3.2245$, $\beta_{2,2} = 1.2$, $A_o = 1$, $\epsilon_d = 1.45$, $\epsilon_1 = 1.3$, and $\epsilon_2 = 1.1$, $\gamma_{th} = 5$ dB, $p = 0.5$, and $q = 1$. For the clear ocean and the coastal ocean, $c(\lambda) = 0.1514\,\mathrm{m}^{-1}$ and $0.399\,\mathrm{m}^{-1}$, respectively. The performance of the DT and the RIS-assisted MRR UOWC link is compared in Section 5.1. Next, in Section 5.2, two diversity techniques, SC and MRC, are investigated for improving performance.

5.1. DT and RIS-Assisted MRR UOWC Links

We investigate the performance of the DT and RIS-assisted MRR UOWC links in Figures 2–6 by plotting P_{out}, average BER, and $\overline{C}$ with IM/DD detection under the combined influence of G–G turbulence, PE, and various water types. The results demonstrate that, for the composite channel models under consideration, the clear ocean performs better than the coastal ocean. Furthermore, Figures 2–6 show how the performance of an RIS-assisted MRR UOWC link improves with the number of RIS elements and how many RIS elements are necessary to attain DT (if available) for a specific average SNR.

As shown in Figures 2–5, although clear ocean conditions provide better performance than coastal ones, the outage probability of the DT link decreases to approximately 3×10^{-3} at an average SNR of 50 dB in coastal water, with even lower values observed under clear ocean conditions. In addition, the average BER performance of BPSK degrades to around 10^{-4} at an average SNR of 50 dB when compared to the RIS-assisted case.

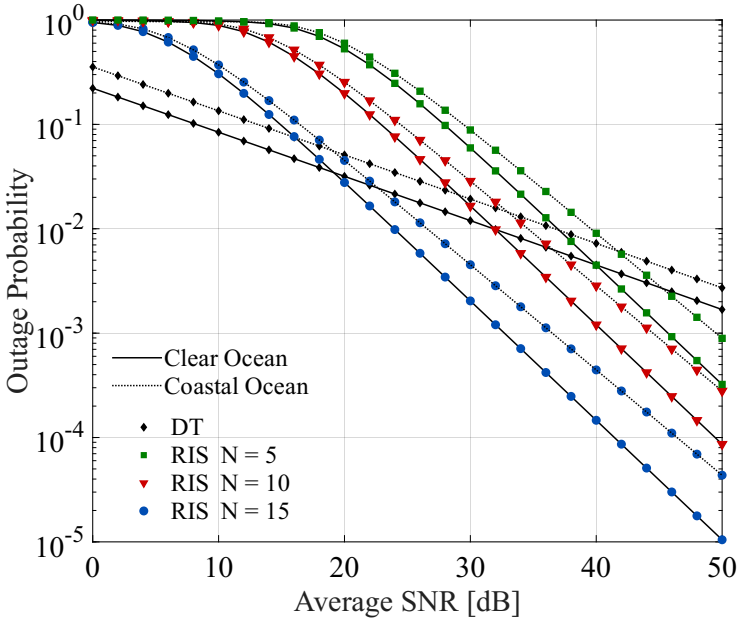

Figure 2. Outage probability versus average SNR in dB for DT and RIS-assisted MRR UOWC links.

Furthermore, both the outage probability and the average BER improve significantly as the number of RIS elements increases. It is also observed that the DT link outperforms the RIS-assisted link at low average SNR values. This behavior can be attributed to the higher

propagation loss (scaling with N) and the impact of short-term fading in the RIS-assisted link compared to the direct transmission case.

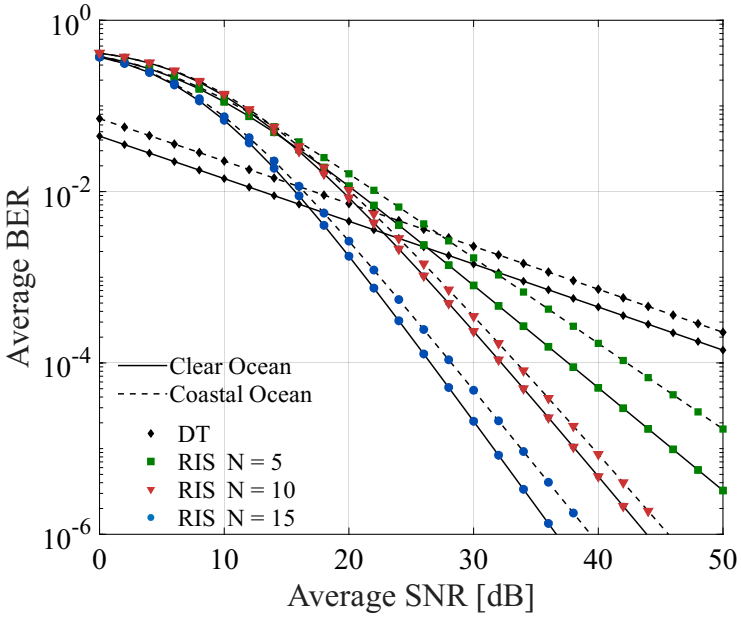

Figure 3. Average BER versus average SNR in dB for DT and RIS-assisted MRR UOWC links.

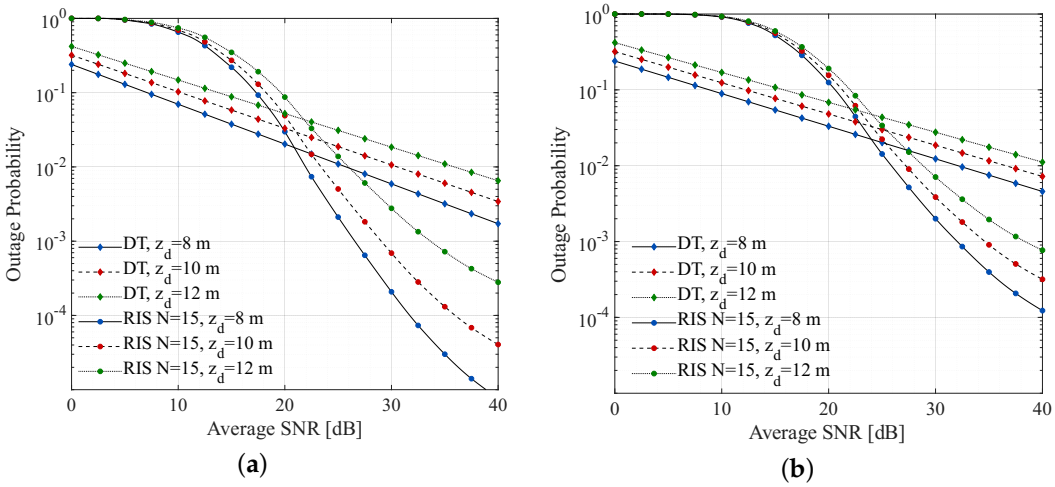

Figure 4. Outage probability versus average SNR in dB for DT and RIS-assisted MRR UOWC links (N = 15) for (**a**) clear ocean and (**b**) coastal ocean.

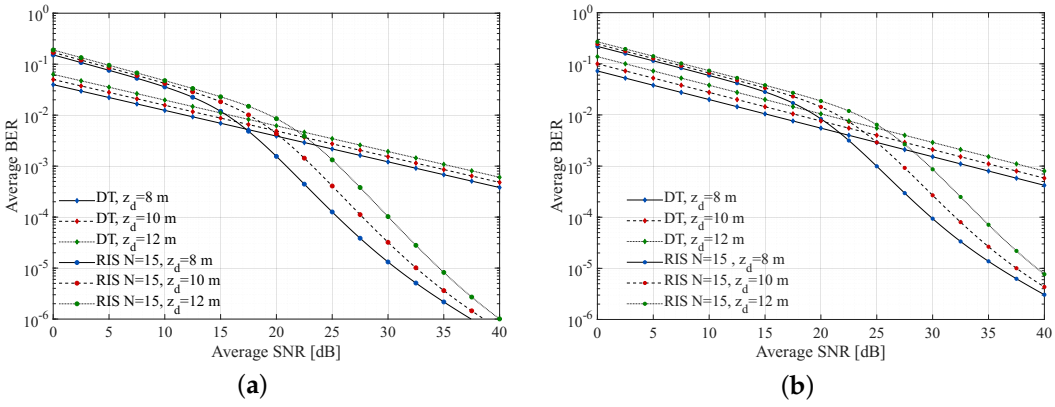

Figure 5. Average BER versus average SNR in dB for DT and RIS-assisted MRR UOWC links (N = 15) for (**a**) clear ocean and (**b**) coastal ocean.

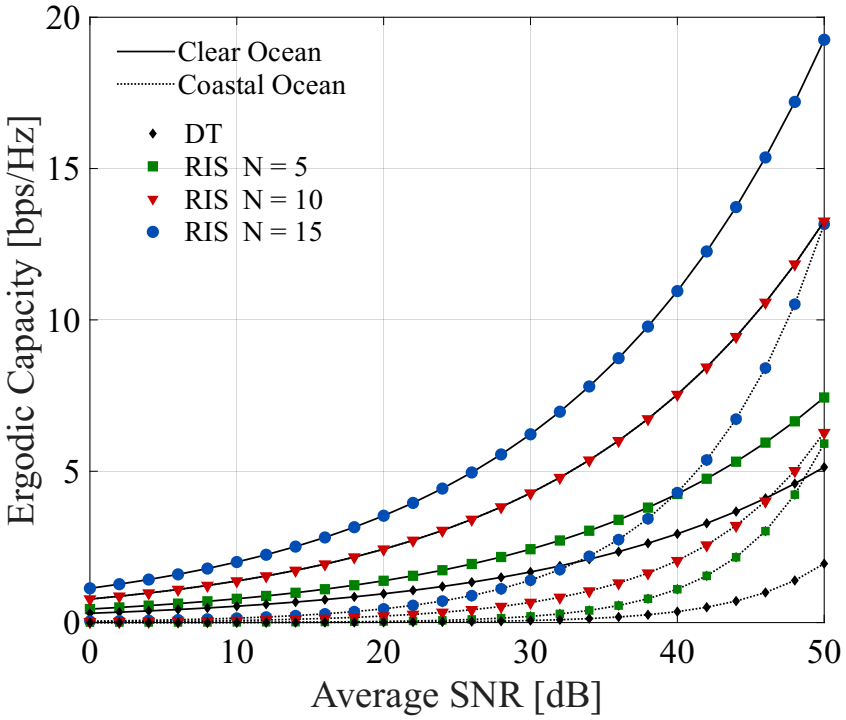

Figure 6. Ergodic capacity in bps/Hz versus average SNR in dB for DT and RIS-assisted MRR UOWC links.

To further quantify this observation, it is clearly seen from Figures 2 and 3 that the RIS-assisted system begins to outperform the DT scheme beyond a specific SNR threshold that depends on both the number of RIS elements and the channel conditions. In particular, under clear ocean conditions, the RIS-assisted link with $N = 15$ surpasses the DT link at approximately 18–20 dB, while for $N = 10$ and $N = 5$, the corresponding transition points occur at approximately 30–32 dB and 38–40 dB, respectively. In coastal ocean environments, these thresholds shift to higher values due to stronger attenuation and scattering effects, occurring approximately at 22 dB, 34 dB, and 42 dB for $N = 15$, $N = 10$, and $N = 5$, respectively.

From a physical perspective, this behavior can be explained by the fact that, at low SNR values, the system performance is dominated by noise and channel impairments, which limits the effectiveness of RIS-assisted transmission. However, as the SNR increases, the RIS provides constructive signal combining and enhances the effective channel gain, leading to a steeper reduction in outage probability compared to the DT scheme.

However, as shown in Figure 2, for a given N, the RIS performance outperforms the DT as average SNR increases. It can be seen that $N = 5$ RIS elements are needed to achieve DT performance at an average SNR of 40 dB, $N = 10$ RIS elements at an average SNR of about 32 dB, and $N = 15$ RIS elements at an average SNR of about 19 dB. Furthermore, as demonstrated in Figure 3, for a given N, the RIS performance outperforms that of DT as average SNR increases. It can be seen that $N = 5$ RIS elements are needed to achieve DT performance at an average SNR of 32 dB, $N = 10$ RIS elements at an average SNR of about 27 dB, and $N = 15$ RIS elements at an average SNR of about 19 dB.

Figure 4 presents the outage probability performance of both the DT and RIS-assisted MRR-UOWC links under clear ocean and coastal ocean conditions. It is observed that, at low SNR values (below approximately 15 dB), the DT link exhibits slightly better or comparable performance compared to the RIS-assisted link. This behavior can be attributed to the fact that, in the low-SNR regime, system performance is dominated by noise rather

than channel enhancements, and thus the additional reflected paths introduced by the RIS do not provide a significant gain.

As the SNR increases, a clear transition region appears where the RIS-assisted link begins to outperform the DT link. Specifically, under clear ocean conditions, the crossover occurs at approximately 18–20 dB for $N = 15$, 30–32 dB for $N = 10$, and around 38–40 dB for $N = 5$. Beyond these thresholds, the outage probability of the RIS-assisted system decreases significantly faster than that of the DT link. For instance, at 50 dB, the outage probability for the RIS-assisted system with $N = 15$ reaches the order of 10^{-5}, whereas the DT link remains around 10^{-3}.

In coastal ocean conditions, a similar trend is observed; however, the crossover points are shifted to higher SNR values due to increased attenuation and scattering. This degradation is mainly caused by the higher extinction coefficient, which reduces the effective received power in both forward and backward paths. Nevertheless, the RIS-assisted system still achieves superior performance at high SNR levels.

Physically, this behavior can be explained by the fact that RIS introduces multiple reflected paths that constructively combine at the receiver. While this gain is negligible in noise-limited conditions, it becomes dominant in moderate-to-high SNR regimes, leading to a substantial improvement in link reliability.

A consistent trend is also observed in Figures 3 and 5 for the average BER performance. In clear ocean conditions, the RIS-assisted link with $N = 15$ surpasses the DT link at approximately 19 dB, while for $N = 10$ and $N = 5$, the transition points occur at around 27 dB and 32 dB, respectively. Similarly, in coastal ocean conditions, these thresholds are observed at approximately 23 dB, 30 dB, and 36 dB. This confirms that the RIS-assisted system becomes increasingly advantageous at moderate-to-high SNR regimes.

This means that increasing the number of RIS elements reduces the transmitted power necessary to achieve DT performance while also offering an alternative channel if LOS between the transceiver and the MRR unit is unavailable. Increasing the transmitted power beyond that value means enhancing the system's performance by decreasing the P_{out} and average BER values.

In addition, in clear water conditions, Figure 2 demonstrates that the $N = 15$ RIS-assisted MRR link achieves a gain of roughly 14 dB of average SNR to attain the same P_{out} of 10^{-3} as the $N = 5$ RIS link. And, as shown in Figure 3, the $N = 15$ RIS-assisted MRR link achieves a gain of around 9 dB of average SNR to attain the same average BER of 10^{-3} as the $N = 5$ RIS link.

Figure 5 illustrates the average BER performance of the DT and RIS-assisted MRR-UOWC links under both clear and coastal ocean conditions. The results show that, similar to the outage probability behavior, the DT link provides comparable or slightly better BER performance in the low-SNR regime. However, as the SNR increases, the RIS-assisted system exhibits a significant improvement in BER performance.

In clear ocean conditions, the RIS-assisted link with $N = 15$ begins to outperform the DT link at approximately 18–20 dB, achieving a BER reduction of nearly two orders of magnitude at high SNR values. For example, at 50 dB, the BER for the RIS-assisted system reaches approximately 10^{-6}, whereas the DT link remains around 10^{-4}. For lower RIS element counts ($N = 10$ and $N = 5$), the improvement is still evident but occurs at higher SNR thresholds, consistent with the outage probability results.

Under coastal ocean conditions, the BER curves shift upward due to stronger channel impairments; however, the same qualitative behavior is maintained. The RIS-assisted system continues to outperform the DT link at sufficiently high SNR values, confirming the robustness of the proposed architecture.

From a physical perspective, the BER improvement arises from the enhanced effective SNR achieved through constructive signal combining via the RIS. As the number of reflecting elements increases, the aggregated channel gain becomes stronger, reducing the probability of bit errors. This demonstrates that RIS not only improves reliability (outage) but also enhances detection accuracy (BER), particularly in challenging underwater environments.

Figure 6 shows that comparing the clear ocean to the coastal ocean, for an average SNR of 50 dB, the $\overline{C}$ increases by 3 bps/Hz for the DT MRR link. In addition, we study the effect of the number of RIS elements on the $\overline{C}$ for clear and coastal oceans with the IM/DD technique. It is evident that as the number of RIS elements increases, so does $\overline{C}$. When we compare the $\overline{C}$ of the RIS-assisted MRR link to that of the DT MRR link, we can see that a 15-element RIS surface can significantly boost spectral efficiency by 13 bps/Hz.

Importantly, the identified SNR thresholds fall within practical operating ranges, demonstrating the feasibility and effectiveness of RIS-assisted MRR-UOWC systems in realistic underwater communication scenarios.

5.2. Diversity Techniques

As shown in Figures 7–9, even at low SNR, RIS combined with DT always performs better than RIS alone (without DT). Thus, it is evident that the combined system performance outperforms that of individual links by utilizing both the signal received through RIS at high SNRs and the existence of DT at low SNRs. The performance at a high average SNR and with a RIS with a huge number of elements is significantly enhanced by the combined effect of RIS and DT.

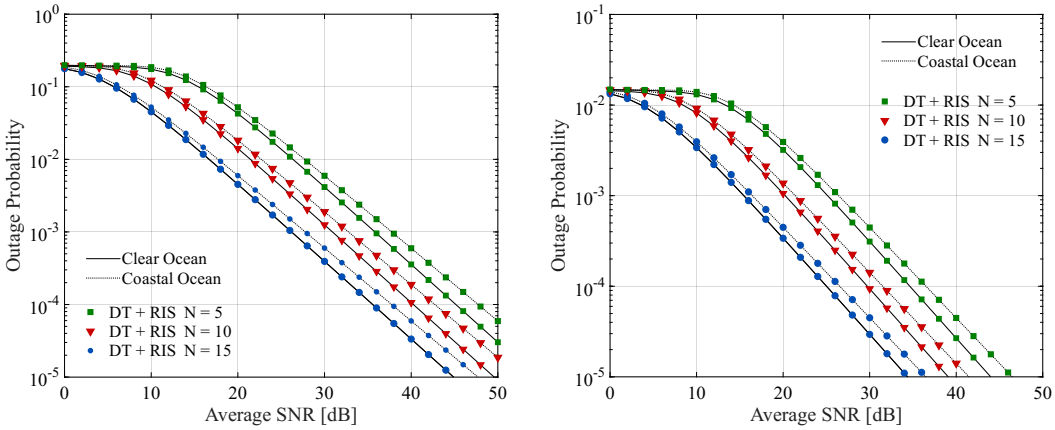

Figure 7. Outage probability versus average SNR in dB for (**a**) SC and (**b**) MRC.

As shown in Figure 7, the comparison of SC and MRC revealed that MRC performs more efficiently at higher average SNR values than SC for certain P_{out} (for example, the MRC receiver reaches a lower outage probability of 10^{-3} at 16 dB, whereas the SC receiver requires the same P_{out} at 27 dB in clear water with $N = 15$ RIS elements). The comparison of SC and MRC in Figure 8 shows that MRC performs efficiently at higher average SNR values than SC for target BERs (for example, an MRC receiver reaches a lower BER of 10^{-3} at 4 dB than the range of an SC receiver, which achieves the same BER at 19 dB in clear water with $N = 15$ RIS elements). In Figure 9, the comparison of SC and MRC shows that MRC performs efficiently at higher average SNR values compared to SC for certain $\overline{C}$ (for instance, an MRC receiver reaches a higher capacity of 20 bps/Hz at 42 dB, whereas the SC receiver reaches the same capacity at 48 dB in clear water with $N = 15$ RIS elements). Of course, the aforementioned results are predicted since MRC processes received signals

from both connections, as opposed to SC, which only processes the link with the highest electrical SNR and so maximizes the output signal's electrical SNR.

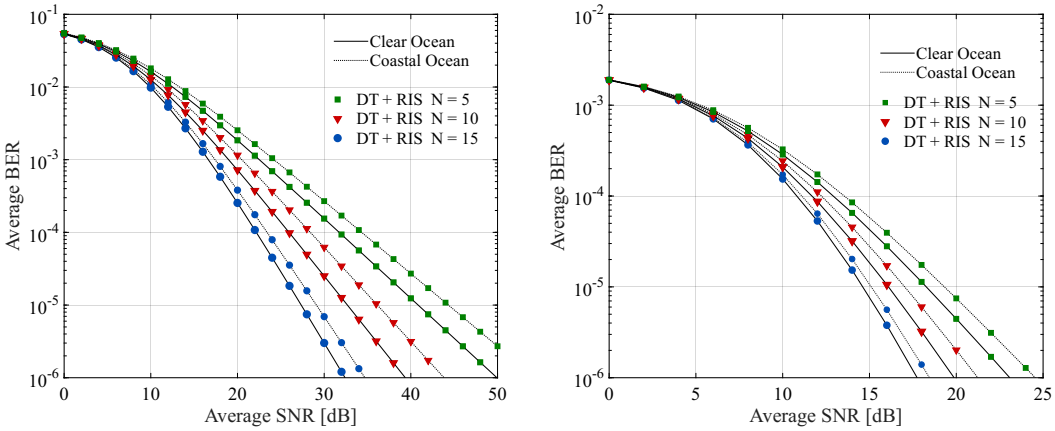

Figure 8. Average BER versus average SNR in dB for (**a**) SC and (**b**) MRC.

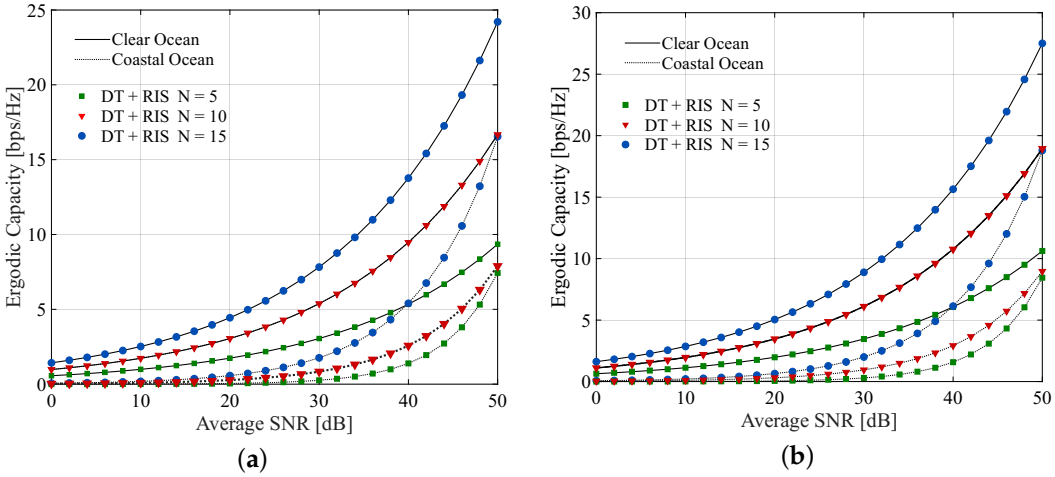

Figure 9. Ergodic capacity in bps/Hz versus average SNR in dB for (**a**) SC and (**b**) MRC.

6. Conclusions

This paper focuses on the use of RIS in MRR UOWC links and how they improve system performance. It provides valuable insights into the performance of such a system. Our results reveal that the number of RIS elements has a significant effect on system performance. Furthermore, the employment of diversity approaches, particularly SC and MRC, is recommended to significantly improve system performance, with MRC performing more efficiently. Achieving optimal performance is critical for successful UOWC applications, and the results of this study emphasize the importance of considering the RIS in UOWC systems. We suggest that relying solely on DT channel studies may not cover all underwater scenarios, and that considering realistic non-line-of-sight behavior in the underwater channel and studying diversity techniques between the DT and RIS-assisted MRR links would have significant implications. In addition to the theoretical contributions, the proposed RIS-assisted MRR-UOWC framework offers significant potential for practical deployment in underwater communication systems. It can be effectively utilized in applications such as environmental monitoring, underwater sensor networks, and offshore exploration, where reliable and energy-efficient communication is essential. The integration of RIS and MRR technologies enables improved link robustness under severe channel impairments, mak-

ing the proposed system a promising solution for next-generation underwater wireless communication scenarios.

Author Contributions: Conceptualization, A.G.A., H.M.S., and K.K.; methodology, A.G.A., A.A., and K.K.; validation, A.G.A.; formal analysis, A.G.A.; investigation, A.G.A., H.M.S., and K.K.; resources, A.G.A. and K.K.; data curation, A.G.A. and A.A.; writing—original draft preparation, A.G.A.; writing—review and editing, A.G.A. and K.K.; visualization, A.G.A., H.M.S., and K.K.; supervision, H.M.S., A.A., and K.K.; project administration, H.M.S. and K.K.; funding acquisition, K.K. All authors have read and agreed to the published version of the manuscript. All authors have read and agreed to the published version of the manuscript.

Funding: This research was funded by the National Institute of Information and Communications Technology (NICT), grant number JPJ012368C09801.

Data Availability Statement: The data supporting the findings of this study are available within the article. Further inquiries can be directed to the corresponding authors.

Conflicts of Interest: The authors declare no conflicts of interest.

References

1. Kaushal, H.; Kaddoum, G. Underwater optical wireless communication. *IEEE Access* **2016**, *4*, 1518–1547.
2. Elfikky, A.; Boghdady, A.I.; AbdElkader, A.G.; Elsayed, E.E.; Palitharathna, K.W.; Ali, Z.; Singh, M.; Mohsan, S.A.H.; Mahmoud, M.; Aly, M.H. Performance analysis of convolutional codes in dynamic underwater visible light communication systems. *Opt. Quantum Electron.* **2024**, *56*, 55.
3. Zeng, Z.; Fu, S.; Zhang, H.; Dong, Y.; Cheng, J. A survey of underwater optical wireless communications. *IEEE Commun. Surv. Tutorials* **2016**, *19*, 204–238.
4. Ho, T.H. *Pointing, Acquisition, and Tracking Systems for Free-space Optical Communication Links*; University of Maryland: College Park, MD, USA, 2007.
5. Quintana, C.; Wang, Q.; Jakonis, D.; Oberg, O.; Erry, G.; Platt, D.; Thueux, Y.; Faulkner, G.; Chun, H.; Gomez, A.; et al. A high speed retro-reflective free space optics links with UAV. *J. Light. Technol.* **2021**, *39*, 5699–5705.
6. Yang, G.; Li, C.; Li, J.; Geng, H.; Bi, M.; Fan, B.; Wang, T. Performance analysis of full duplex modulating retro-reflector free-space optical communications over single and double gamma-gamma fading channels. *IEEE Trans. Commun.* **2018**, *66*, 3597–3609.
7. Mohamed, P.H.; El-Shimy, M.A.; Shalaby, H.M.; Kheirallah, H.N. Hybrid FSO/RF system over proposed random dust attenuation model based on real-time data combined with G–G atmospheric turbulence. *Opt. Commun.* **2023**, *549*, 129891.
8. Sajmath, P.; Ravi, R.V.; Majeed, K.A. Underwater wireless optical communication systems: A survey. In *Proceedings of the 2020 7th International Conference on Smart Structures and Systems (ICSSS)*; IEEE: New York, NY, USA, 2020; pp. 1–7.
9. ElMossallamy, M.A.; Zhang, H.; Song, L.; Seddik, K.G.; Han, Z.; Li, G.Y. Reconfigurable intelligent surfaces for wireless communications: Principles, challenges, and opportunities. *IEEE Trans. Cogn. Commun. Netw.* **2020**, *6*, 990–1002.
10. AbdElKader, A.G.; Allam, A.; Kato, K.; Shalaby, H.M. Performance enhancement of RIS-assisted MRR-UOWC systems using the spectral-power-efficient LQAM-MPPM. *Opt. Commun.* **2024**, *559*, 130444.
11. AbdElKader, A.G.; Allam, A.; Kato, K.; Shalaby, H.M. Performance analysis of a UAV-integrated RIS-aided MRR-FSO system utilizing wavelength and time diversity techniques. *Photonic Netw. Commun.* **2025**, *50*, 1.
12. Dabiri, M.T.; Hasna, M.; Althunibat, S.; Qaraqe, K. Modulating retroreflector-based satellite-to-ground optical communications: Acquisition, sensing, and positioning. *IEEE Trans. Commun.* **2024**, *73*, 483–497.
13. Chen, C.; Ji, J.; Zhao, H.; Song, Y. Performance analysis and experimental evaluation of modulating retroreflector and UAV based free space optical transmission systems. *Opt. Express* **2024**, *32*, 33830–33851.
14. Rosenkrantz, E.; Arnon, S. An innovative modulating retro-reflector for free-space optical communication. In *Proceedings of the Laser Communication and Propagation Through the Atmosphere and Oceans II*; SPIE: Bellingham, WA, USA, 2013; Volume 8874, pp. 57–65.
15. Yang, G.; Li, Z.; Bi, M.; Zhou, X.; Zeng, R.; Wang, T.; Li, J. Channel modeling and performance analysis of modulating retroreflector FSO systems under weak turbulence conditions. *IEEE Photonics J.* **2017**, *9*, 7902610.
16. Kudathanthirige, D.; Gunasinghe, D.; Amarasuriya, G. Performance analysis of intelligent reflective surfaces for wireless communication. In *Proceedings of the ICC 2020–2020 IEEE International Conference on Communications (ICC)*; IEEE: New York, NY, USA, 2020; pp. 1–6.
17. Selimis, D.; Peppas, K.P.; Alexandropoulos, G.C.; Lazarakis, F.I. On the performance analysis of RIS-empowered communications over Nakagami-m fading. *IEEE Commun. Lett.* **2021**, *25*, 2191–2195.

18. Jamali, V.; Ajam, H.; Najafi, M.; Schmauss, B.; Schober, R.; Poor, H.V. Intelligent reflecting surface assisted free-space optical communications. *IEEE Commun. Mag.* **2021**, *59*, 57–63.
19. Trigui, I.; Ajib, W.; Zhu, W.P. A comprehensive study of reconfigurable intelligent surfaces in generalized fading. *arXiv* **2020**, arXiv:2004.02922.
20. Yang, L.; Guo, W.; Ansari, I.S. Mixed dual-hop FSO-RF communication systems through reconfigurable intelligent surface. *IEEE Commun. Lett.* **2020**, *24*, 1558–1562.
21. Wang, J.; Zhang, W.; Bao, X.; Song, T.; Pan, C. Outage analysis for intelligent reflecting surface assisted vehicular communication networks. In *Proceedings of the GLOBECOM 2020-2020 IEEE Global Communications Conference*; IEEE: New York, NY, USA, 2020; pp. 1–6.
22. Kong, L.; He, J.; Ai, Y.; Chatzinotas, S.; Ottersten, B. Channel modeling and analysis of reconfigurable intelligent surfaces assisted vehicular networks. In *Proceedings of the 2021 IEEE International Conference on Communications Workshops (ICC Workshops)*; IEEE: New York, NY, USA, 2021; pp. 1–6.
23. Chapala, V.K.; Zafaruddin, S.M. RIS-assisted multihop FSO/RF hybrid system for vehicular communications over generalized fading. *arXiv* **2021**, arXiv:2112.12944.
24. Zhang, Q.; Yue, D.W.; Xu, X.Y. Performance analysis of reconfigurable intelligent surface-assisted underwater wireless optical communication systems. *IEEE Photonics J.* **2024**, *16*, 7301914.
25. Heydaribeni, A.; Beyranvand, H. Performance analysis of underwater optical wireless communication using O-RIS and fiber optic backhaul (extended version). *arXiv* **2025**, arXiv:2508.18915.
26. AbdElKader, A.G.; Allam, A.; Kato, K.; Shalaby, H.M. Performance Enhancement of MRR Underwater Optical Communications Using LQAM-MPPM. In *Proceedings of the 2022 Asia Communications and Photonics Conference (ACP)*; IEEE: New York, NY, USA, 2022; pp. 473–476.
27. Du, H.; Zhang, J.; Cheng, J.; Ai, B. Millimeter wave communications with reconfigurable intelligent surfaces: Performance analysis and optimization. *IEEE Trans. Commun.* **2021**, *69*, 2752–2768.
28. Mohamed, P.H.; El-Shimy, M.A.; Shalaby, H.M.; Kheirallah, H.N. FSO Channel Modelling and Performance Evaluation Over Dust Combined With GG Atmospheric Turbulence. In *Proceedings of the 2023 40th National Radio Science Conference (NRSC)*; IEEE: New York, NY, USA, 2023; Volume 1, pp. 121–130.
29. Farid, A.A.; Hranilovic, S. Outage capacity optimization for free-space optical links with pointing errors. *J. Light. Technol.* **2007**, *25*, 1702–1710.
30. Jung, K.J.; Nam, S.S.; Alouini, M.S.; Ko, Y.C. Unified finite series approximation of FSO performance over strong turbulence combined with various pointing error conditions. *IEEE Trans. Commun.* **2020**, *68*, 6413–6425.
31. Research, W. The Mathematical Functions Site. 1998. Available online: https://functions.wolfram.com (accessed on 8 August 2023).
32. Mathai, A.M.; Saxena, R.K.; Haubold, H.J. *The H-Function: Theory and Applications*; Springer Science & Business Media: New York, NY, USA, 2009.
33. Hai, N.; Srivastava, H. The convergence problem of certain multiple Mellin-Barnes contour integrals representing H-functions in several variables. *Comput. Math. Appl.* **1995**, *29*, 17–25.
34. Peppas, K.P. A new formula for the average bit error probability of dual-hop amplify-and-forward relaying systems over generalized shadowed fading channels. *IEEE Wirel. Commun. Lett.* **2012**, *1*, 85–88.